Contents lists available at ScienceDirect

International Journal of Solids and Structures

journal homepage: www.elsevier.com/locate/ijsolstr

Pneumatically tunable adherence of elastomeric soft hollow pillars with non-circular contacts

Guangchao Wan, Wanliang Shan *

Department of Mechanical and Aerospace Engineering, Syracuse University, Syracuse, NY 13244, USA

ARTICLE INFO

Keywords:
Tunable adhesion
Buckling instability
Interfacial delamination
Soft hollow pillars
Pneumatics

ABSTRACT

Dynamically tunable interfacial dry adhesion plays a significant role in numerous biological functions and industrial applications. Among various strategies, pneumatics-activated adhesive devices draw much attention due to their distinct advantages such as fast speed, reliable performance, large adhesion tunability and easily accessible materials. To understand and predict adhesion strength of pneumatics-activated adhesives, it is necessary to examine their interfacial mechanics that is nonlinearly coupled with the large deformation of the devices under pressure. However, previous studies have only focused on axisymmetric cases in which the outline of the contact area is circular, whereas the tunable adherence of non-circular contact controlled by pneumatics remains elusive. In this work, through a combination of experiments and simulations, we study the effect of non-circular contact geometry on tunable dry adhesion of pressure-activated soft hollow pillars. Specifically, elliptical, square, and rectangular contact shapes are considered and their effects on tunable adhesion of the soft hollow pillars are compared to that of circular contact geometry thoroughly. The results show that soft hollow pillars with elliptical, square, and rectangular contact surfaces demonstrate rich interfacial delamination behaviors that depend on the contact outline geometry and internal pressure. Among all contact geometries, elliptical contact has the highest adhesion tunability yet requires lowest activating pressure owing to the non-uniform curvature distribution of the contact outline. However, when the eccentricity increases, the elliptical contact has reduced tunability of adhesion caused by the contact of opposing sides of the sidewall upon buckling. For square and rectangular contacts, they have the lowest adhesion tunability and need higher activating pressure than those of circular and elliptical contact since the 90-degree edges of the sidewall prohibit buckling instability. Our findings greatly broaden the design space of pneumatics-activated adhesive devices by adding the contact geometry of the soft hollow pillars as a new design parameter, which can provide valuable guidance for tunable adhesive design for various applications in manufacturing and robotics.

1. Introduction

The ability to dynamically regulate interfacial adhesion on demand proves vital to numerous biological performance (Autumn et al., 2000; Yao and Gao, 2006) and industrial applications including locomotion of micro-robots (Wu et al., 2022), micro-transfer printing (Kim et al., 2010; Meitl et al., 2006), robotic manipulation (Coulson et al., 2021; Luo et al., 2022a), wound healing (Chen et al., 2022), etc. Of particular interest is to realize tunable dry adhesion in an efficient manner. To address such a challenge, there have been efforts in fabricating smart adhesive structures whose adhesive strength varies when subjected to external stimuli. These designs exploit various forms of external stimuli including mechanical forces (Carlson et al., 2011; Deneke et al., 2023; Johannes et al., 2022; Zhang et al., 2022), magnetic field (Drotlef et al., 2014; Testa et al., 2020; Wang et al., 2023; J. Zhao et al., 2022), electric current (Mohammadi Nasab et al., 2022; Tatari et al., 2018), temperature (Linghu et al., 2023, 2020), light (Ma et al., 2018; Wang et al., 2020), etc. to change the shape, modulus, or surface morphology of the adhesive devices to control adhesive strength. Among these activation strategies, pneumatics (air pressure) has its advantages including fast speed (Swift et al., 2020), reliable performance (B. Haverkamp et al., 2021), large adhesion tunability (Song and Sitti, 2014) and easily accessible materials.

For pneumatics-activated adhesive devices, there are two major working mechanisms. One is to rely on the "suction" effect in which vacuum space is created above the target surface so that the adhesive

---

* Corresponding author.
E-mail address: washan@syr.edu (W. Shan).

https://doi.org/10.1016/j.ijsolstr.2024.112736
Received 26 August 2023; Received in revised form 19 January 2024; Accepted 21 February 2024

device is pressed against the target surface through pressure difference (Frey et al., 2022; Koivikko et al., 2021). The highest adhesion strength due to suction is thus the atmospheric pressure (1 bar). Once the vacuum seal is breached, the adhesion drops significantly. The other mechanism utilizes dry adhesion between the target surface and a flat contact membrane to generate high adhesion strength. Above the contact membrane there exists an internal air chamber whose sidewall deforms when the pressure inside the chamber changes. The deformation of the sidewall and the contact membrane alters the interfacial stress distribution and thereby changes the adhesive strength. The adhesion strength of such a working mechanism is usually lower than that of the suction cup design. However, since it does not require good sealing as suction effect does, its adhesion performance is less sensitive to the roughness and curvature of the target surface and thus attracts much attention. To name a few, Carlson, et al. devised a microscale elastomeric stamp that can achieve $\sim 50 \times$ switching ratio using positive pressure ~ 50 kPa (Carlson et al., 2012). Here, the term “switching ratio” refers to the ratio of the highest over the lowest adhesion strength of the device. In this study, the air pressure inflates the bottom contact membrane and detaches the membrane from the target surface. A more recent study by Swift, et al. used a combination of negative and positive pressure in which positive pressure inflates the bottom membrane for adhesion reduction and detachment while negative pressure enhances adhesion through modulus regulation to further increase the switching ratio to $1000\times$ (Swift et al., 2020). Mimicking Gecko’s toe pad, Tian, et al. employed pneumatics to inflate or deflate an array of enclosed elastomeric chambers to pick and place flat objects (Tian et al., 2019). In addition to these methods relying on the deformation of the contact membrane subjected to internal pressure, a different strategy was proposed by Mohammadi Nasab, et al. who made use of subsurface air pressure to bend both the sidewall and contact membrane of the adhesive device to regulate the interfacial stress distribution (Mohammadi Nasab et al., 2020). The designed gripper can reach $\sim 7 \times$ change of dry adhesion with a maximum adhesion strength up to 67 kPa. Most recently, a novel concept named soft hollow pillars (SHPs) has been introduced by Wan, et al. to realize two orders of magnitude change of dry adhesion based on air pressure as low as ~ 10 kPa by exploiting shell buckling instability (Wan et al., 2022).

The failure of dry adhesion can be explained using linear elastic fracture mechanics models. The Griffith criterion states that the interfacial delamination initiates and propagates when the energy release rate is equal to the critical energy release rate (Jagota and Hui, 2011). Therefore, to understand and predict the adhesive behaviors of these elastomeric adhesive structures, it is necessary to examine their contact mechanics, which is affected by multiple factors including the work of adhesion (Plaut et al., 2003), large deformation (Long and Hui, 2012), elastomer thickness (Bartlett and Crosby, 2014; Wan and Duan, 2002), curvature (Shi et al., 2011), interfacial cavitation (Areyano et al., 2021), and stiffness (Minsky and Turner, 2017, 2015; Tian et al., 2022). To address the complexities of such a highly nonlinear mechanics problem, one efficient strategy is to calculate the energy release rate of the elastomeric gripper through either theoretical analysis (Long et al., 2010; Swift et al., 2020; Wahdat et al., 2021; Wan, 2001; Yang et al., 2023) or numerical simulation (C. Zhao et al., 2022). The interfacial delamination is then determined by the Griffith criterion. In addition to the energy method, dry adhesion can also be predicted by analyzing the contact stress distribution. The formation of interfacial cracks occurs when local contact stress meets the failure criterion (Balijepalli et al., 2016; Hensel et al., 2018; Luo et al., 2022b). For instance, Mohammadi Nasab, et al. employed simulations based on finite element method (FEM) to determine the contact stress distribution and explain adhesion enhancement under internal positive pressure (Mohammadi Nasab et al., 2020). Apart from contact stress analysis, one can also build an interfacial cohesive model to monitor delamination. For instance, Wan, et al. used cohesive interaction based on FEM to predict the adhesive force and contact area evolution during interfacial delamination when SHPs are activated by internal pressure (Wan et al., 2022). These studies have predominantly focused on axisymmetric cases where the perimeter of the contact surface is circular. However, the effect of the non-circular shape of the contact outline on adhesive performance, which is inherently a 3D problem, remains largely unexplored. The adoption of non-circular contact surface for solid adhesive pillars offers certain advantages such as high packing density (Luo et al., 2020; Xue et al., 2017), easy fabrication (Murphy et al., 2009), good shape match between the target object and the gripper (Meitl et al., 2006; Minsky and Turner, 2017), and directional adhesion (Cho et al., 2018; Kwak et al., 2011; Wang et al., 2015). Therefore, investigating the non-circular contacts of pneumatics-controlled adhesion not only deepens our understanding of adhesive behaviors but also provides new design flexibility that can potentially benefit the fabrication and application of such devices.

In this work, we focus on SHPs, which are a novel class of elastomeric adhesive structures, and study their pneumatics-tunable adherence to flat surfaces when the contact outline is elliptical, square, or rectangular, in comparison with the circular case that has been studied before. As shown in Fig. 1(a), a SHP features a tube-like sidewall with one end sealed by a flat contact membrane and the other end connected to a pressure source so that the internal pressure p can be controlled on demand. Here, pressure is defined as the deviation from atmospheric pressure. A positive (negative) pressure value signifies that the internal pressure exceeds (is lower than) atmospheric pressure. The geometrical parameters of a SHP include the height denoted as h, the thickness of the top membrane denoted as t_p, and the thickness of the sidewall and bottom membrane denoted as t_s and t_b, respectively. We exemplify the working principle based on a circular SHP. When the internal pressure is zero, the SHP exhibits strong adhesion when adhered to a flat surface, allowing for the successful lifting of an object from the substrate (Fig. 1(a)). Releasing the object could be achieved through the application of either positive or negative pressure. When positive pressure is applied, the bending of the sidewall initiates interfacial delamination within the contact area near the edge, leading to adhesion reduction. Conversely, the application of negative pressure induces buckling instability in the hollow pillar. The sidewall buckles inwards, forming two dimples that face each other in space. Simultaneously, the bottom membrane deforms into a saddle shape and detaches itself from the target surface. As a result, the adhesion is significantly reduced due to the loss of contact area.

The contour of contact is dictated by the shape of the contact membrane, which can be circular, elliptical, square, or rectangular, as illustrated in Fig. 1(b). The circular contact membrane has a diameter represented by d, while the elliptical contact membrane is defined by the semi-major axis, a, and the semi-minor axis, b. In the case of a square or rectangular contact membrane, its length and width are denoted by l and w, respectively. Through a combination of experiments and finite element simulations, we examine the adhesion strength and interfacial delamination behaviors of these SHPs as internal pressure changes. The results show that SHPs with all contact geometries exhibit rich interfacial delamination behaviors, - and that the interfacial delamination initiation location shifts as pressure changes (Fig. 1(b)). In general, for all contact geometries, the delamination can start from the contact edge or inside the contact area depending on the applied internal pressure. Particularly, for circular or elliptical contacts, delamination can be induced by buckling instability when internal pressure is negative with large enough magnitude. However, such a behavior is absent in square or rectangular contacts. For edge delamination, the initiation location can be the vertexes or the co-vertexes in elliptical contacts, and the corners or the midpoints of straight edges in square and rectangular contacts. When internal pressure is positive and large enough, SHPs with all contact geometries develop internal delamination. Regarding tunable adhesion performance, it is found that the elliptical contact geometry with small eccentricity has the optimal performance including the highest adhesion tunability ($\sim 182 \times$), the lowest activating pressure (~ 8 kPa) and well-controlled buckling directions.

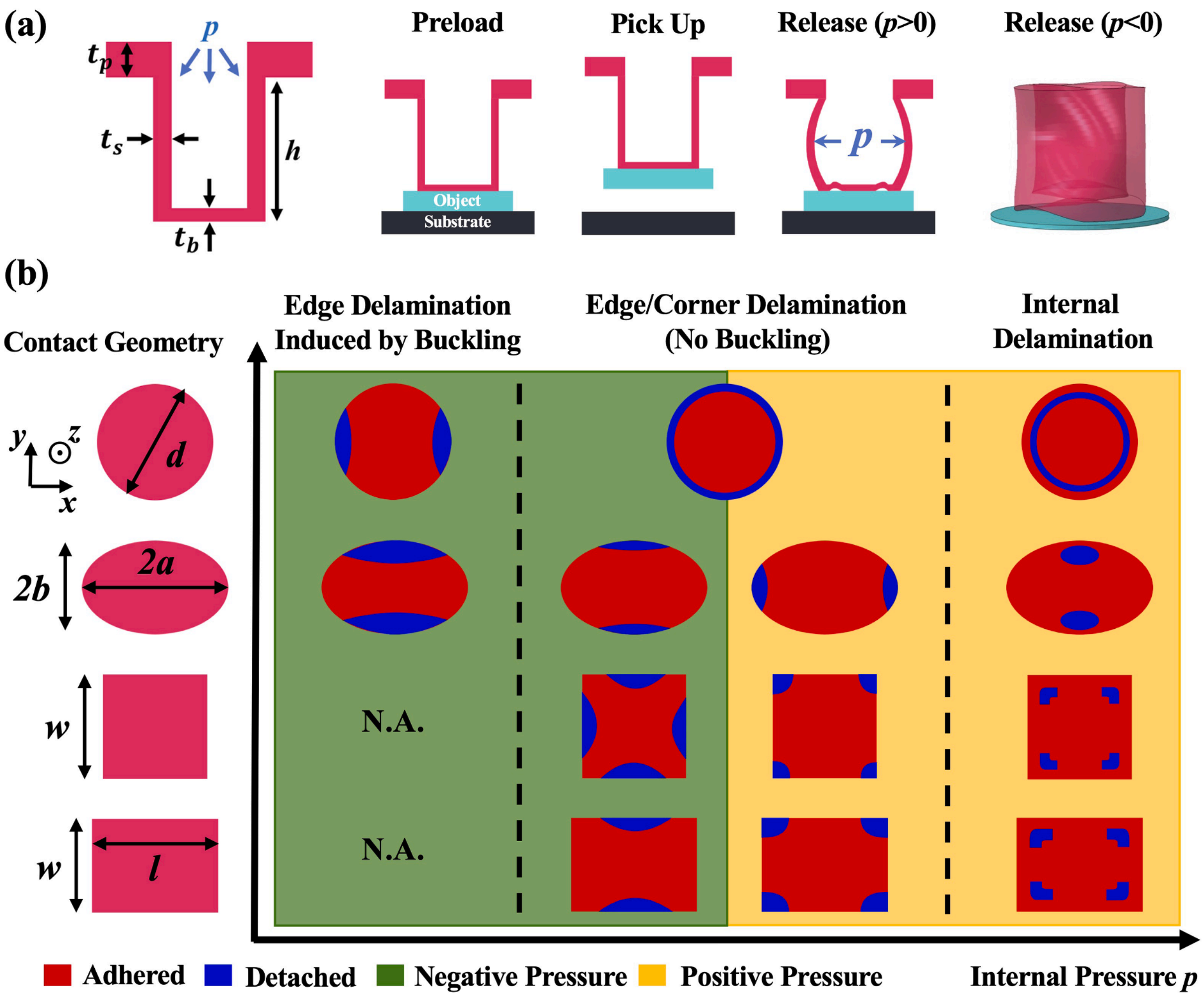

Fig. 1. (a) Schematic illustrations of a SHP of circular contact geometry and its working mechanism for tunable dry adhesion under positive and negative pressure. (b) Summary of interfacial delamination behaviors of SHPs with circular, elliptical, square, and rectangular contact geometries under negative and positive pressure.

The rest of the paper is organized as follows. Section 2 introduces the experimental setup and simulation framework that are used to examine the adhesive behaviors of SHPs. Section 3 and Section 4 present the adherence SHPs of elliptical, square, and rectangular contact geometries, respectively. Section 5 discusses the advantages and disadvantages of circular, elliptical, square, and rectangular contact geometries in terms of activating pressure, adhesion tunability and controlled buckling behaviors. Some concluding remarks are provided in Section 6.

2. Research methods

The adhesion properties of the SHP against a flat substrate are influenced by its geometric parameters, as exemplified in the circular contact scenario (Wan et al., 2022). Consequently, to investigate the effect of the contact outline's shape on adhesion performance, the effects of these geometric parameters should be controlled, and thus all scenarios in this study maintain consistent values for these dimensions: the SHP has a fixed height of $h = 6$ mm, sidewall thickness $t_s = 0.8$ mm, bottom membrane thickness $t_b = 0.8$ mm, and top membrane thickness of $t_p = 2$ mm. Furthermore, considering that the tensile force is primarily carried by the sidewall when the contact membrane adheres to the substrate, it is crucial to maintain consistency in the projected area of the sidewall on the contact plane. This area can be approximated by the product of the sidewall thickness, t_s, and the circumference, c, of the contact membrane. In the meanwhile, the adhesion strength is less sensitive to other geometric parameters such as height h. Therefore, for a fair comparison of contact shape effect on adhesion strength of SHPs, all samples in this study are designed to have an identical circumference, denoted as $c \approx 18.8$ mm. These geometric parameters are chosen to ensure good dimensional accuracy of 3D printed molds and facilitate mold release in SHP fabrication. Using another set of geometric parameters can quantitatively change the adhesion performance. For instance, the pull-off strength σ_p without applied pressure ($p = 0$ kPa) and buckling pressure p_c increase with a larger sidewall thickness t_s and smaller contact circumference c. However, the adhesion tunability, in which we are mostly interested, stays consistent qualitatively. Therefore, the chosen set of geometric parameters is sufficient to illustrate the adhesion behaviors of SHPs with various contact shapes.

2.1. *Experimental measurement of dry adhesion of SHPs*

The SHPs used in this study are made of polymers vinylpolysiloxane (VPS, Elite Double 8, Zhermack) and were fabricated through the mold casting method. The mold's geometry is precisely controlled through 3D printing (Objet30 Prime, Stratasys). To minimize roughness of the contact membrane and ensure optimal contact with a flat target surface, the curing process involves pressing the contact membrane of the SHPs against a glass piece with a smooth surface, as depicted in Fig. 2(a). Once the SHP is successfully fabricated, it is affixed to a 3D printed fixture using uncured VPS as glue. The fixture is then firmly attached to an Instron Miro-Tester (Model 68SC1) that controls the movement of the SHP and measures the interactive force with the substrate (Fig. 2(b)).

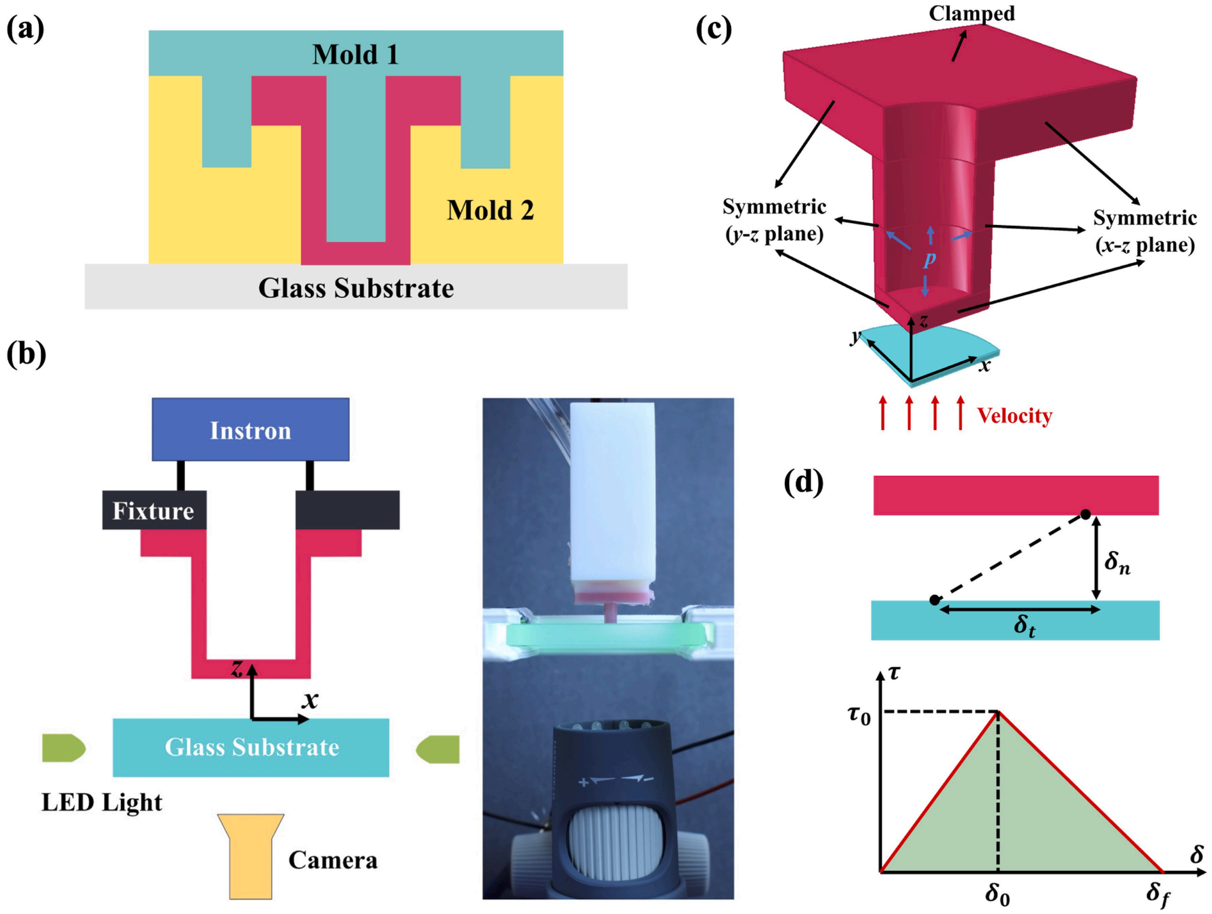

Fig. 2. (a) Schematic illustration of the mold-casting fabrication of SHPs with different contact geometries. (b) Schematics and photo of experimental setup for measuring adhesive force and capturing contact area evolution of a SHP. (c) Geometric model and boundary conditions for FEM simulations. (d) Traction-separation law in cohesive interaction for FEM simulations.

The Instron machine is equipped with a load cell featuring a measurement precision of 1 mN and a capacity of 5 N.

To quantify the dry adhesion between the SHP and a flat glass substrate, a specific experimental procedure is followed. The SHP first approaches the substrate with a constant velocity of 1 mm/min. The motion stops when the compressive force between the SHP and the glass substrate reaches 200 mN. This force threshold is chosen to ensure proper contact between the contact membrane and the glass substrate, as supported by previous work (Wan et al., 2022). Once the contact is established, the SHP remains stationary for two minutes. During this period, the internal pressure p is adjusted to a desired value, which is measured using a digital manometer (range ~ 70 kPa, resolution 0.01 kPa). Positive pressure is applied using a pressure source, while negative pressure is controlled through a syringe. Following the stationary period, the SHP retracts from the glass substrate at a constant speed of 0.2 mm/min until complete detachment is achieved. Throughout the retraction process, the internal pressure p is kept constant. The Instron machine records both the location of the SHP, denoted as z, and the interactive force with the substrate, represented as F, during the entire test. The variable z is set as zero when the SHP first contacts the substrate, and the force F is positive (negative) when the interaction between the SHP and the substrate is compressive (attractive) (Fig. 2(b)). The pull-off force F_p, used as a measure of adhesion strength, is determined as the maximum attractive force observed during the retraction process. Accordingly, the pull-off strength σ_p is defined as the pull-off force F_p divided by the total area of the contact membrane. At least three measurements are conducted for adhesion strength at each internal pressure level. Both the average and the standard deviation of the pull-off force are reported. In addition to tracking the force–displacement relationship, the contact area between the SHP and the substrate during the separation is monitored using two LED lights positioned at the lateral sides of the substrate. The phenomenon of light scattering (Tinnemann et al., 2019) allows the adhered area to appear bright, while the detached area appears dark. This technique enables the visualization and analysis of the formation and propagation of interfacial delamination during the experiment. To calculate the switching ratio and activating pressure under both positive and negative pressure regimes, the pull-off strength without pressure ($p = 0$ kPa) is used as the highest adhesive strength, and the plateau value of the adhesion strength under large enough pressure magnitude is used as the lowest adhesion strength. Moreover, the activating pressure is taken as the lowest pressure magnitude beyond which adhesion strength plateaus.

2.2. *Modeling the adhesive behaviors using FEM*

In addition to experimental measurement, FEM based on the commercial software ABAQUS is employed to provide insight for the adhesion behaviors of the SHP. Through simulations, we can quantitatively examine the effects of deformations in the sidewall and the contact membrane on adhesion strength and identify the contact stress distribution that governs the initiation site of interfacial delamination.

3D finite element analysis is performed for all cases. Experimental observations indicate that the SHP exhibits mirror symmetry during both inflation and deflation with respect to the two principal planes. To reduce computational cost, only a quarter of the SHP is modeled, and symmetric boundary conditions are applied at the principal planes

(Fig. 2(c)). This approach allows for a more efficient simulation while preserving the essential characteristics of the SHP's adhesive behaviors.

The VPS material is modelled using the incompressible Neo-Hookean constitutive model. The parameters are set asC_{10} = 0.041 MPa, D_1=0 MPa^{-1}, obtained from experimental tensile testing on VPS. The glass substrate is modeled as linear elastic with a Young's modulus of 1000 MPa and a Poisson's ratio of 0.3. To simulate the experimental procedure, a dynamic implicit analysis is conducted, following the approach-contact-retract sequence. The top surface of the SHP is clamped to replicate its tight adherence to the 3D printed fixture. Meanwhile, the rigid substrate is moved towards or away from the contact membrane at a constant speed (Fig. 2(c)). The simulation parameters such as the moving speed, contact force and contact time are kept identical to those used in the experiment. It is worth mentioning that during the "approach" step, a positive pressure with negligible magnitude (1 kPa) is applied within the SHP to inflate the contact membrane a little so that an intact contact can be formed with the substrate. The SHP is divided into 8-node linear hybrid elements with reduced integration (C3D8RH). The mesh size is chosen as 0.05 ~ 0.075 mm at the contact interface after a mesh convergence study. Further decreasing the mesh size at the interface will change the adhesive force by less than 0.5 %.

To model the dry adhesion, we assigned the cohesive interaction between the contact membrane and the glass substrate based on the surface-surface contact formulation. This cohesive response is allowed during repeated post-failure contact. Previous studies have demonstrated the capability of cohesive interaction in modelling interfacial adhesion (Hwang et al., 2023; Li et al., 2022) and friction (Cen and Komvopoulos, 2023; Glover et al., 2023). Specifically, the adhesive force between two contacting surfaces is described using a bi-linear traction-separation law as depicted in Fig. 2(d). Details of the cohesive interaction setup in ABAQUS can be found in Appendix A.

3. Adhesion of elliptical contact

In this section, we explore the adhesive behaviors of SHPs with an elliptical contact outline. Compared to circular contact, the introduction of eccentricity to the contact outline breaks the rotational symmetry and introduces new features in both sidewall deformation and dry adhesion. Details of circular contact can be found in our previous work (Wan et al., 2022) and Appendix B. We focus on two representative sets of geometric parameters. Both cases have the same sidewall thickness (t) and circumference (c). However, they differ in eccentricity e with values of 0.64 and 0.87, and the eccentricity e is defined as $\sqrt{1-(b/a)^2}$, where a and b are the semi-major axis and the semi-minor axis.

3.1. Elliptical contact with eccentricity $e = 0.64$

We first study the dry adhesion of an SHP of an elliptical contact when its eccentricity $e = 0.64$. As demonstrated in the circular contact case (Appendix B), the sidewall deformation plays a crucial role in the adhesion performance. Thus, it is essential to first investigate the deformation of an elliptical SHP to gain insights into its adhesive performance. Quantitatively, we use simulations to extract the displacement of two specific points on the sidewall when the internal pressure is varied. At the same time, we put displacement constraint on the contact surface of the bottom membrane as this interface is adhered to the target surface. These specific points are positioned in the middle along the height direction (z direction) and are located at the vertex (point A) and co-vertex (point B) of the elliptical cross section of the SHP (Fig. 3(a)). The displacement of point A along the x direction is denoted as $u_{A,x}$, while the displacement of point B along the y direction is denoted as $u_{B,y}$. As verification, we also perform simulation without adhered constraint and compare it with the shapes of the SHPs under internal pressure in experiments (Fig. 3(c)).

As shown in Fig. 3(a), when the internal pressure is positive, both

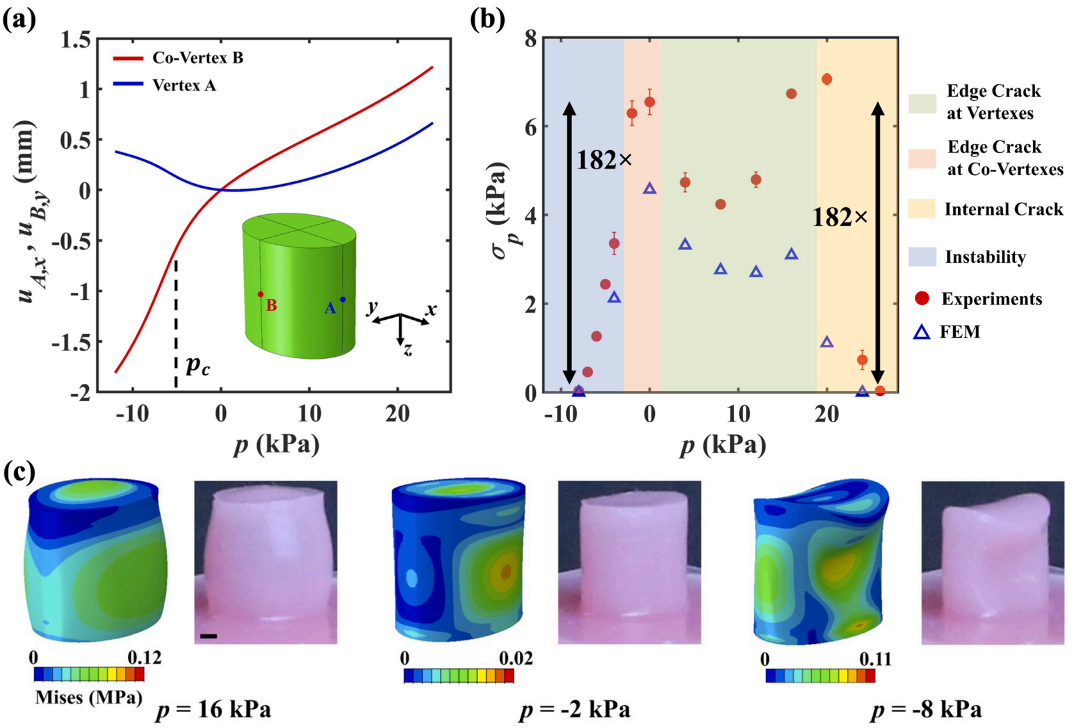

Fig. 3. (a) Displacement of point A (vertex) along x axis $u_{A,x}$ and displacement of point B (co-vertex) along y axis $u_{B,y}$ with internal pressure p in simulations. (b) Relationship between pull-off strength σ_p and internal pressure p of a SHP with elliptical contact geometry ($e = 0.64$) in experiments (red circles) and simulations (blue triangles). The plot is divided into four regimes based on interfacial delamination behaviors. (c) Deformation of an elliptical SHP with $e = 0.64$ under internal pressure $p = 16$ kPa, -2 kPa and -8 kPa in simulations (left) and experiments (right). The scale bar is 1 mm.

$u_{A,x}$ and $u_{B,y}$ are positive. This indicates that the sidewall of the elliptical SHP bulges outwards at both its vertex and covertex positions. Particularly, the displacement at the co-vertexes $u_{B,y}$ is larger than those at the vertexes $u_{A,x}$, which implies that the sidewall experiences more significant bending around its co-vertexes under positive pressure. This phenomenon becomes apparent in an example scenario when $p = 16$ kPa (Fig. 3(c), left).

When the internal pressure p becomes negative, $u_{B,y}$ becomes negative while $u_{A,x}$ remains positive. Furthermore, the magnitudes of both $u_{B,y}$ and $u_{A,x}$ increase with higher pressure magnitudes (Fig. 3(a)). The opposite signs of $u_{B,y}$ and $u_{A,x}$ indicate that the sidewall bends inwards around its co-vertexes while bending outwards around its vertexes. Accordingly, two tiny dimples are formed in the sidewall as exemplified when $p = -2$ kPa (Fig. 3(c), middle). It is important to note that this deformation, characterized by the formation of dimples, is a result of the SHP's geometry rather than buckling instability as observed in a buckled circular SHP.

The slope of the p - $u_{B,y}$ curve becomes steep when the pressure magnitude exceeds $p_c = 4$ kPa, indicating the occurrence of buckling instability (Fig. 3(a)). Upon buckling, the sidewall further collapses inwards around its co-vertexes, and the contact membrane deforms into a saddle shape without the adhered constraint ($p = -8$ kPa, Fig. 3(c)). To estimate the buckling pressure p_c of an elliptical SHP, we assume that buckling is initiated by the local deformation at the co-vertexes and thereby depends on the local circumferential curvature. For a circular SHP, the buckling pressure follows the scaling law $p_c \sim \rho^{3/2}$ when material properties and other geometric parameters are held constant (Wan et al., 2022), where ρ is the circumferential curvature of the sidewall's neutral surface. Based on this equation, the estimated value of p_c is approximately 5 kPa, which is close to the simulation results.

The non-uniform sidewall deformation of an elliptical SHP under internal pressure has a significant impact on its adhesive behaviors. The relationship between the pull-off strength σ_p and internal pressure p is presented in Fig. 3(b), revealing four qualitatively distinct interfacial delamination behaviors (Figs. 4, 6). These behaviors are classified based on the initiation locations of the interfacial crack, including the vertexes, co-vertexes, or inside the contact area. Furthermore, the delamination induced by the buckling instability is classified as a new behavior, as it introduces new features in both delamination propagation and the p - σ_p relationship.

Edge Crack at Vertexes

When the internal pressure p is positive and lower than 20 kPa, interfacial delamination initiates at the vertexes of the contact outline. This edge crack is unstable and quickly propagates towards the whole interface once it starts ($p = 8$ kPa, Fig. 4(a)). To determine the pull-off strength, we extract the relationship between interactive force F and SHP's location z during the adhesion test in both experiments and simulations. As shown in Fig. 4(a), during the adhesion test, the SHP first approaches the substrate, and the interaction force F is compressive (positive) and gradually increases as the location, z, decreases. After the "approach" step, the SHP reaches a stationary state with a constant location, z, and the internal pressure p is applied. As a result, the compressive force continues to increase due to the applied internal pressure. Finally, the SHP retracts from the substrate, resulting in an increase in the location z. During this step, the interaction force F transitions from compressive to attractive (negative). The magnitude of the attractive force progressively increases until it reaches the pull-off force, and then quickly decreases to zero as the interface fails quickly when delamination begins. In this regime ($0 \text{ kPa} < p < 20 \text{ kPa}$), the pull-off strength σ_p exhibits a non-monotonic relationship with pressure p. In experiments, σ_p initially decreases from 6.55 kPa to 4.24 kPa when the internal pressure p increases from 0 kPa to 8 kPa. Then σ_p increases to 7.06 kPa when the pressure p further increases to 20 kPa.

The non-monotonic change of the pull-off strength with internal pressure variation and the interfacial delamination behavior can be

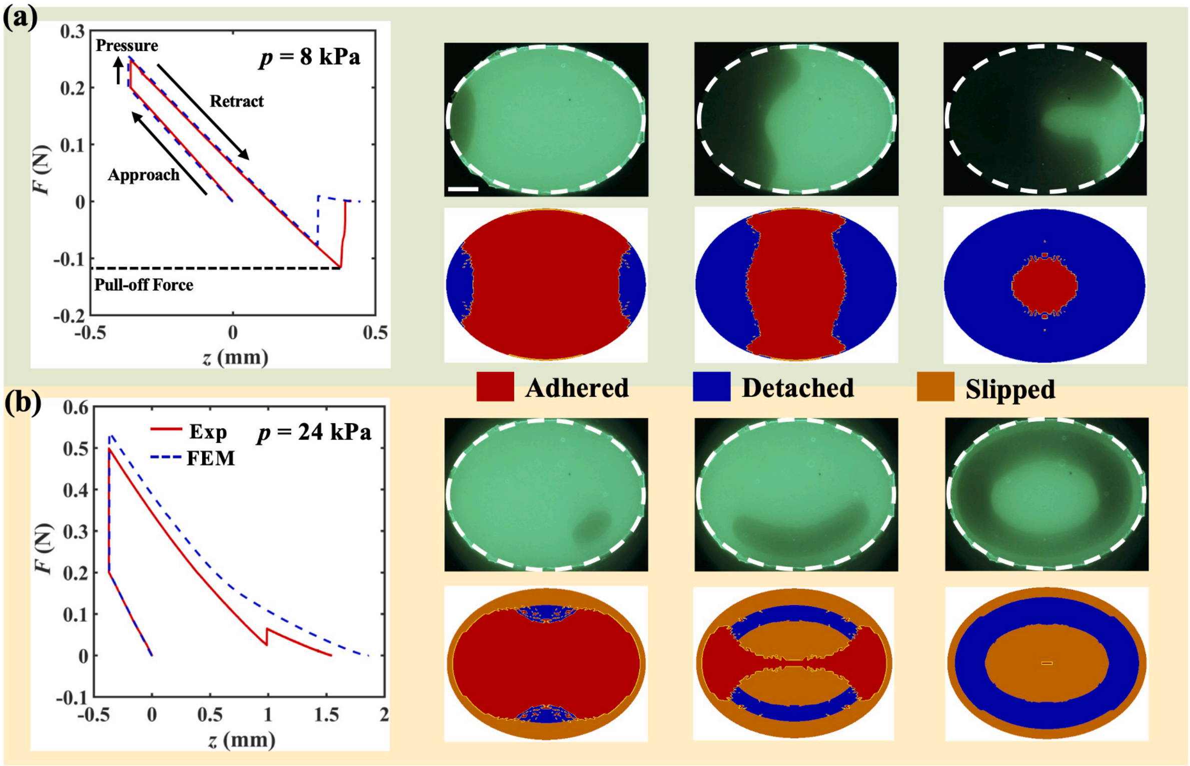

Fig. 4. Force F - displacement z curve and contact area evolution during adhesion test in both experiment (red solid curve) and simulation (blue dashed curve) for elliptical contact geometry ($e = 0.64$) under positive pressure, including (a) edge crack at vertexes ($p = 8$ kPa) and (b) internal crack ($p = 24$ kPa). The white dash line marks contact outline in experiment in the first row, and the simulation is shown in the second row. The scale bar is 1 mm.

explained by examining the contact normal stress distribution when interfacial delamination starts. Specifically, we study three representative cases when $p = 0$, 8 and 16 kPa. As shown in Fig. 5(a), when $p = 0$ kPa, the contact normal stress is higher at the contact edge than inside the contact area. Particularly, along the contact outline, contact stress is highest at vertexes than other positions because vertexes have the largest circumferential curvature and act like sharp corners in solid pillars (Luo et al., 2020). When p increases to 8 kPa, the highest contact stress remains at vertexes. However, the contact stress appears compressive around the co-vertexes and inside the contact area (Fig. 5 (a)). Such contact stress distribution is caused by the non-uniform sidewall bending. As seen in the circular contact (Appendix B), the outward bending deformation of the sidewall reduces the contact stress level at edge. In the meanwhile, for an elliptical SHP, its sidewall deforms the least around its vertexes. These two combined factors indicate that vertexes have the highest contact stress along the contact outline. Since the pull-off force is the integration of the contact normal stress over the contact area, the existence of compressive stress suggests a reduced pull-off strength.

As the internal pressure increases further to 16 kPa, the sidewall bending becomes significant everywhere along the contact outline. Accordingly, the formation of edge crack is delayed at both the co-vertexes and the vertexes. At the same time, a ring-shape region with high tensile stress is developed inside the contact area (Fig. 5(a)), and the pull-off force increases. By examining the contact normal stress distribution along the semi-major axis (Fig. 5(b)), we observed a tensile contact stress peak near the edge when $p = 16$ kPa, reminiscent of circular contact under high positive pressure.

Inner Crack along the Minor Axes

When the internal positive pressure is higher than 20 kPa, interfacial delamination begins to initiate inside the contact area rather than at the edge ($p = 24$ kPa, Fig. 4(b)). In this case, the contact stress reaches its peak at the minor axes near the co-vertexes since the sidewall bends most significantly there (Fig. 5(a)). Once the internal crack is formed, it first slowly grows within the ring-shape region with high contact stress inside the contact area when the SHP retracts. Then it propagates towards the contact edge, leaving only the central area adhered to the substrate. Finally, the crack front spreads towards the contact area's center until the interface completely fails. Such a stable crack growth suggests a smooth variation of interactive force F during the adhesion test (Fig. 4(b)), and the pull-off strength σ_p decreases rapidly to a negligible value of $\sigma_p = 0.036$ kPa when the internal pressure p increases to 26 kPa in experiments (Fig. 3(b)). Using the adhesion strength with zero internal pressure as the reference highest value of 6.55 kPa, the switching ratio is calculated to be 182 × in the positive pressure regime, and the activating pressure that triggers the sharp decline in adhesion strength is 26 kPa.

Edge Crack at Co-vertexes

When the internal pressure is negative with a magnitude below the buckling pressure (-4 kPa $< p < 0$ kPa), the interfacial crack initiates at the co-vertexes and rapidly propagates throughout the entire contact area ($p = -2$ kPa, Fig. 6(a)). Under negative pressure, the inward bending of the sidewall facilitates edge delamination (Fig. B1(b)). Therefore, the delamination starts at the co-vertexes because the sidewall deforms most here. In this regime, the pull-off strength σ_p decreases slightly to 6.29 kPa as the pressure magnitude increases to 2 kPa (Fig. 3(b)) in experiments.

Buckling-induced Edge Crack at Co-vertexes

Once the magnitude of the negative pressure surpasses the critical value of $p_c = 4$ kPa, the sidewall of the SHP buckles, which forces the contact membrane to detach from the substrate. Since two dimples are always formed around the co-vertexes, the interfacial delamination still initiates at the co-vertexes. However, this buckling-induced delamination exhibits two distinct characteristics. First, the pull-off strength σ_p decreases significantly with increasing pressure magnitude, dropping below 0.036 kPa when $p = -8$ kPa (Fig. 3(b)) in experiments. This abrupt decline in adhesion strength synchronizes with the steep slope of the p - $u_{B,y}$ curve in Fig. 3(a), indicating that the adhesion is reduced due to the sidewall collapse of the buckled SHP. Second, unlike the unstable interfacial crack that quickly propagates in the third delamination type, the crack propagates with two stages in this case. In the first stage, two edge cracks form at the co-vertexes immediately upon the application of pressure and they rapidly approach each other ($p = -8$ kPa). However, the crack fronts do not meet in the middle of the contact area. Instead, a thin elongated interfacial region develops along the major axis between the two vertexes, remaining adhered (Fig. 6(b)). This behavior contrasts with circular SHPs, where the two interfacial cracks merge (Fig. B2)). Then the second stage begins as the interfacial crack becomes stable. As retraction continues, this adhered region gradually becomes thinner. At a certain moment, the two crack fronts finally meet each other rapidly around the focus of the elliptical outline, splitting the adhered region. It

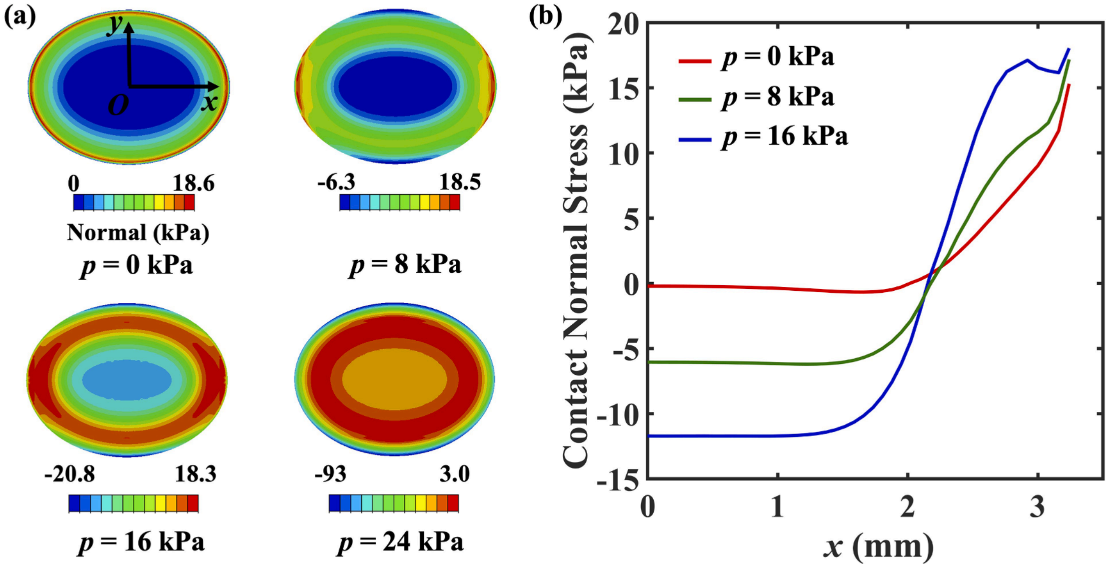

Fig. 5. (a) Contact normal stress distribution over elliptical contact area ($e = 0.64$) when internal pressure p is 0 kPa, 8 kPa, 16 kPa and 24 kPa in FEM simulations. (b) Contact normal stress distribution along the semi-major axis of elliptical contact area ($e = 0.64$) when internal pressure p is 0 kPa, 8 kPa and 16 kPa in FEM simulations.

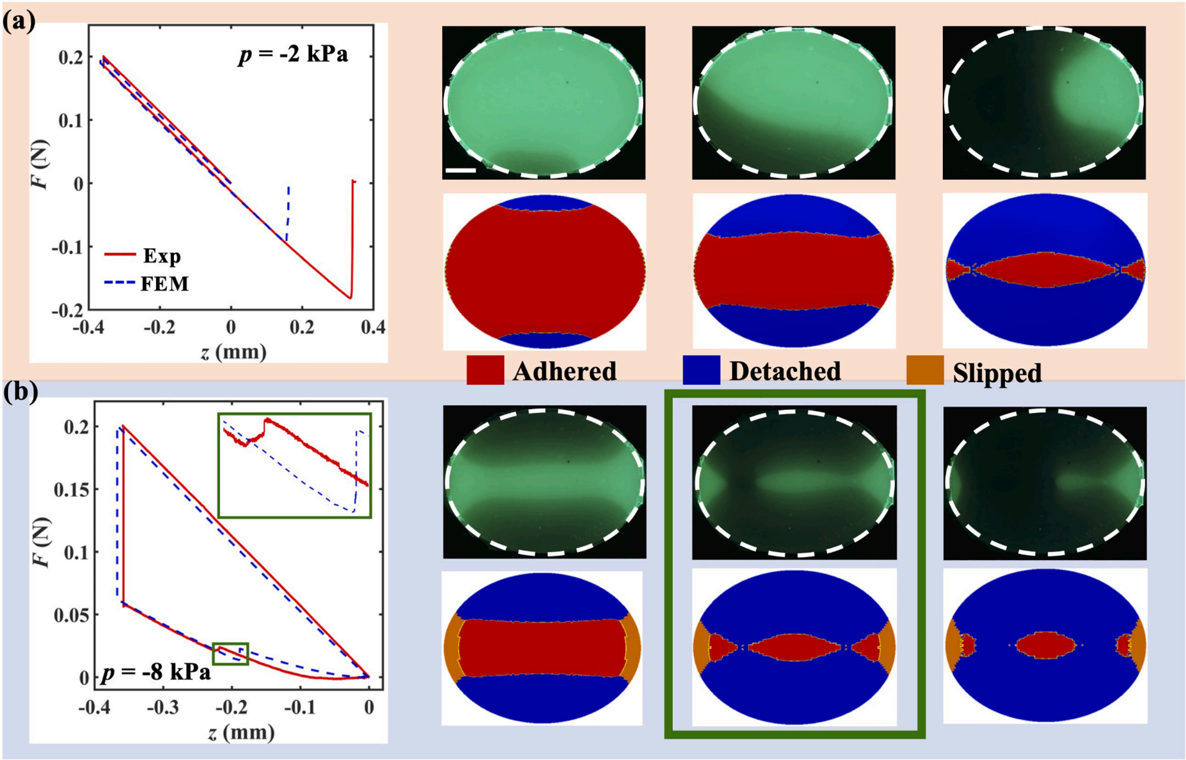

Fig. 6. Force F - displacement z curve and contact area evolution during adhesion test in both experiment (red solid curve) and simulation (blue dashed curve) for elliptical contact geometry ($e = 0.64$) under negative pressure, including (a) edge crack at co-vertexes (p = -2 kPa) and (b) buckling-induced edge crack (p = -8 kPa). The white dash line marks contact outline in experiment in the first row, and the simulation is shown in the second row. The green box highlights the abrupt change in force. The scale bar is 1 mm.

is also reflected in the $z - F$ curve where a sudden change of interactive force F is observed (Fig. 6(b), green box). As the retraction further proceeds, the area of the adhered region shrinks until the entire interface fails. Due to the contact area loss at the end of the first stage of interfacial delamination propagation, the pull-off strength σ_p falls below measurement precision in experiment (0.036 kPa). Accordingly, the switching ratio is determined to be 182×, and the activating pressure is identified as 8 kPa when the internal pressure is negative.

As depicted in Figs. 3–6, the FEM results have successfully captured various experimental observations, such as the deformation of the SHPs, the z - F relationship, the pull-off strength σ_p, and the evolution of the contact area. However, the simulated pull-off strength σ_p consistently appears lower than the experimental measurements. This discrepancy arises from the fact that chosen parameters in the cohesive interaction model are unable to fully represent the dry adhesion observed in the experiments. Given our intention to utilize simulation as a qualitative tool to explain changes in adhesion and interfacial delamination behaviors, we did not engage in a trial-and-error process to adjust the parameters in the cohesive interaction model for a quantitative match. Such parameter calibration would involve significant computational cost.

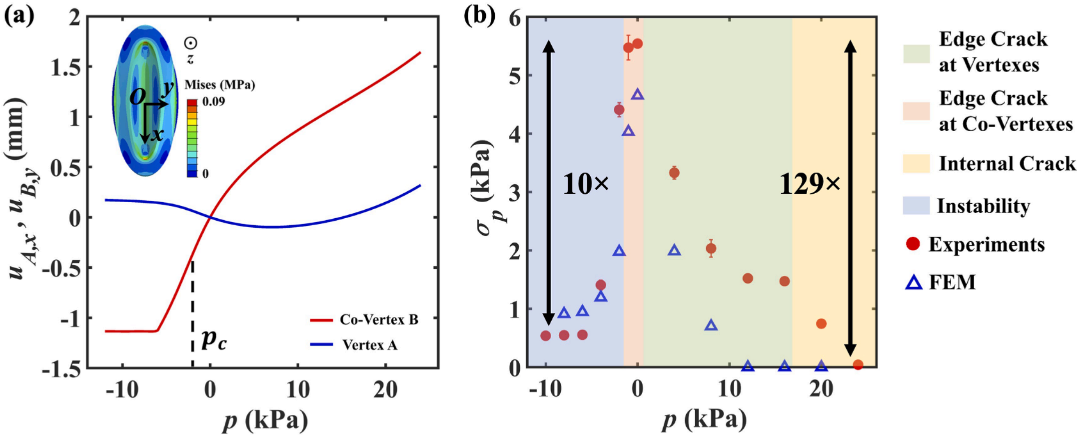

Fig. 7. (a) Displacement of point A (vertex) along x axis $u_{A,x}$ and displacement of point B (co-vertex) along y axis $u_{B,y}$ with internal pressure p in FEM simulations. Inset is the self-contact of sidewall in FEM simulations (p = -8 kPa). (b) Relationship between pull-off strength σ_p and internal pressure p of a SHP with elliptical contact geometry ($e = 0.87$) in experiments (red circles) and simulations (blue triangles). The plot is divided into four regimes based on the interfacial delamination behaviors.

3.2. Elliptical contact with eccentricity $e = 0.87$

To examine the consistency of these adhesive behaviors, we study another elliptical contact configuration with a larger eccentricity, $e = 0.87$. Following the same investigation paradigm as before, we begin by characterizing the sidewall bending under internal pressure. Fig. 7(a) shows the results obtained from simulations for displacement of two points on the sidewall (point A, vertex; point B, co-vertex) under internal pressure. It can be observed that the sidewall bends outward around the co-vertexes under positive pressure, as indicated by the positive displacement, $u_{B,y}$. However, around the vertexes, the sidewall bends inwards when the positive pressure is low ($u_{A,x}$ is negative). Only when the positive pressure exceeds a certain threshold ($p > 16$ kPa) does the sidewall begin to bend outward.

Because of the increased eccentricity, the buckling pressure p_c is further reduced to 1.8 kPa through theoretical estimation. Therefore, the slope of the p - $u_{B,y}$ curve exhibits a rapid increase when the pressure p becomes negative due to the early onset of buckling instability (Fig. 7 (a)). Before buckling, the sidewall still bends inward around the co-vertexes while bending outward around the vertexes (p = -1 kPa, Fig. C1), similar to the behavior observed in the elliptical SHP with $e = 0.64$. As the pressure magnitude increases, both $u_{A,x}$ and $u_{B,y}$ rapidly reach plateaus when p = -6 kPa. At this stage, the two dimples of the

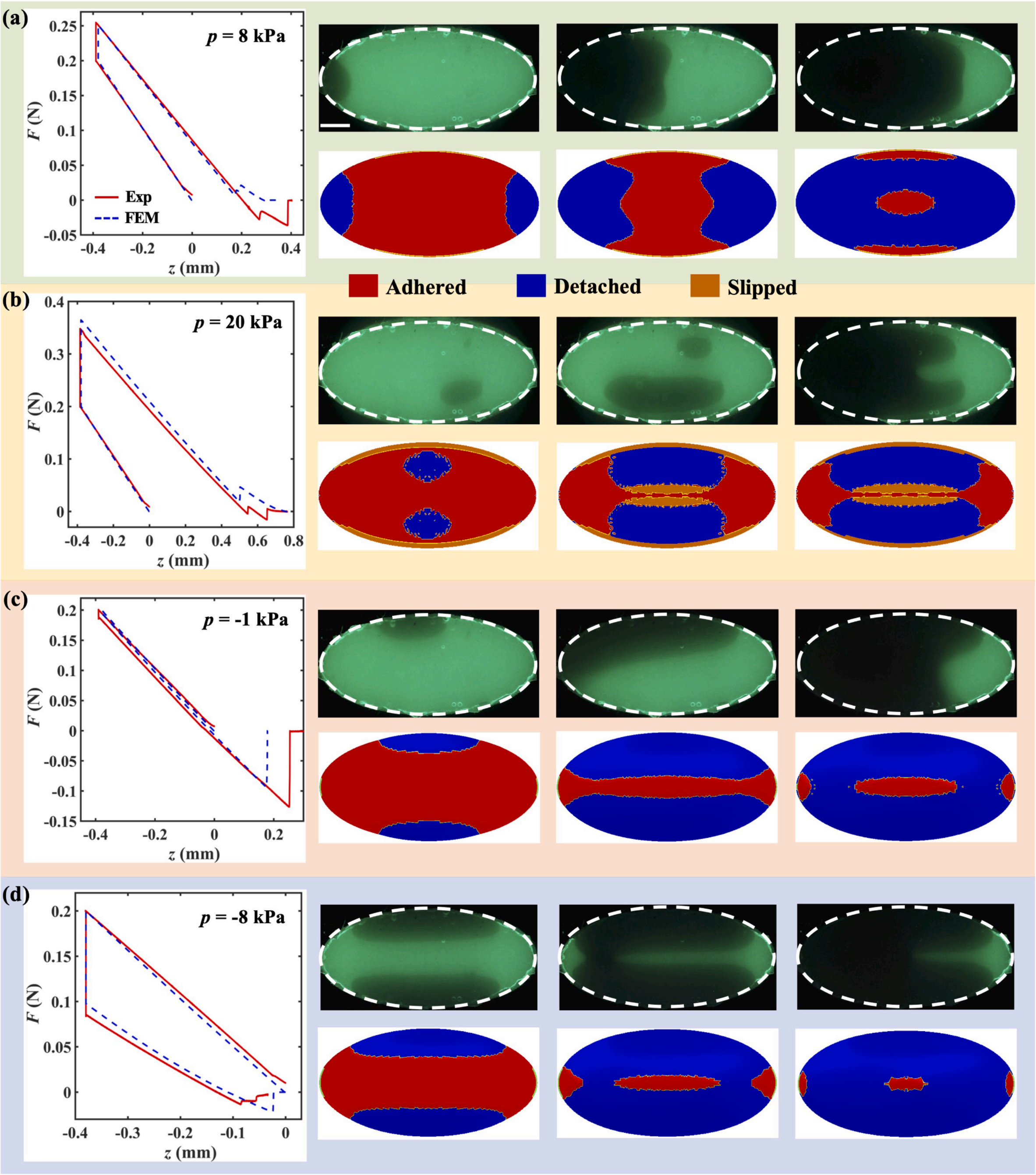

Fig. 8. Force F - displacement z curve and contact area evolution during adhesion test in both experiments (red solid curves) and simulations (blue dashed curves) for elliptical contact geometry ($e = 0.87$). Four interfacial delamination behaviors are (a) edge crack at vertexes ($p = 8$ kPa), (b) internal crack ($p = 20$ kPa), (c) edge crack at co-vertexes ($p = -1$ kPa), and (d) instability-induced interfacial crack ($p = -8$ kPa). The white dash curve makes elliptical contact outline in experiment in the first row, and simulation is shown in the second row. The scale bar is 1 mm.

buckled SHP begin to touch each other, preventing further bending of the sidewall, as demonstrated in the inset of Fig. 7(a) when p = -8 kPa. This early occurrence of sidewall self-contact comes from the short minor axis of the elliptical outline.

The presence of a larger eccentricity in an SHP introduces new features to its adhesion behaviors. While the same four interfacial delamination behaviors are observed (Fig. 8), the relationship between pressure p and pull-off strength σ_p displays a distinct trend (Fig. 7(b)). Specifically, in the regime where delamination initiates at the vertexes (0 kPa $< p <$ 16 kPa, Fig. 8(a)), σ_p keeps decreasing from 5.54 kPa to 1.47 kPa as p increases from 0 kPa to 16 kPa in experiments, which is different from the non-monotonic variation observed when $e = 0.64$. The underlying reason is that the sidewall bends inward rather than outward at the vertexes when $p <$ 16 kPa. Therefore, the interface is always weakened at the vertexes by sidewall bending, leading to a reduction in pull-off strength. When $p >$ 16 kPa, the interfacial delamination starts inside the contact area near the co-vertexes as the contact stress becomes highest there (Fig. 8(b), Fig. C2). Similar to the elliptical contact with $e = 0.64$, the internal crack propagates slowly with retraction and σ_p is reduced below 0.043 kPa when p is raised to 24 kPa in experiments, leading to a switching ratio of 129 ×.

Due to the low buckling pressure p_c, the third interfacial behavior, in which delamination starts at co-vertexes (p = -1 kPa, Fig. 8(c)), exists within a narrow range of internal pressure (-2 kPa $< p <$ 0 kPa). In this regime, σ_p slightly decreases with pressure magnitude increase (Fig. 7 (b)) under the same reason as elliptical contact with $e = 0.64$. When internal pressure reaches the buckling pressure $p_c \approx$ 2 kPa, σ_p begins to drop significantly (Fig. 7(b)). However, unlike the previous case in which σ_p is reduced below measurement precision, in this case, σ_p reaches a plateau around 0.56 kPa when p = -6 kPa, and further raising pressure magnitude does not help decrease adhesion strength anymore as measured in experiments. Accordingly, the switching ratio using negative pressure becomes low as 10 ×. This ineffectiveness in reducing adhesion strength comes from the limited deformation of both sidewall and contact membrane, which results from the sidewall self-contact. As a result, the contact membrane has less tendency to detach itself from the substrate. As shown in Fig. 8(d) when p = -8 kPa, once the buckling begins, only a small portion of contact area is lost near two co-vertexes, and a wide, long region remains adhered along the major axis. This adhered region can bear attractive force to some extent, leading to a low switching ratio.

4. Adhesion of SHPs with square and rectangular contacts

In this section, we investigate the adhesive behaviors of SHPs with a square or rectangular contact outline. One distinct feature of SHPs with a square or rectangular contact is the presence of 90-degree sharp corners along the contact outline and 90-degree sharp edges in the sidewall, which are absent in both circular and elliptical contacts. Previous studies have demonstrated that 90-degree sharp corners along the contact outline promote contact stress concentration (Luo et al., 2020). Therefore, it is expected that, when no pressure is applied, interfacial delamination should initiate at the corners. In addition to sharp corners, a square or rectangular SHP also possesses 90-degree sharp edges in its sidewall. The influence of these sharp edges on the sidewall's deformation under internal pressure and their subsequent impact on the adhesive behaviors remain unknown. The following subsections aim to address these questions.

4.1. Square contact

We begin by examining square contact outline with $l = w = 4.71$ mm. Constrained by four 90-degree sharp edges, the four facets of the sidewall either bend outward or inward under positive or negative pressure in the same manner, respectively, as demonstrated in both experimental observations and finite element simulations (Fig. 9(c)). Furthermore, the sidewall exhibits a greater tendency to bend around the center of the facets than the 90-degree sharp edges. To quantitatively analyze this behavior, we utilize simulation to extract the displacement of the facet's center A along the x direction $u_{A,x}$ with adhered constraint applied. As shown in Fig. 9(a), the smooth variation of $u_{A,x}$ with internal pressure p suggests that SHPs with a square contact do not undergo buckling instability under negative pressure. Instead, the four facets only deform locally. This behavior contrasts sharply with circular or elliptical SHPs. At the same time, constrained by four 90-degree sharp edges, a square SHP has smaller sidewall deformation than an elliptical SHP in terms of displacement magnitude. These unique characteristics play a pivotal role in determining the adhesion of SHPs with square contact. The relationship between the pull-off strength σ_p and internal pressure p is shown in Fig. 9(b). Three types of interfacial delamination behaviors are observed. Specifically, delamination can initiate at the corners, at midpoints of four straight edges, or inside the contact area.

Corner Crack

When internal pressure is positive and below 16 kPa (p = 8 kPa, Fig. 10(a)), the interfacial delamination initiates at the four corners and propagates towards the center of the contact area. The propagation speed is fast once the delamination starts. To gain further insights, FEM simulations are conducted and the contact stress distribution when delamination starts is examined. As illustrated in Fig. 11(a), without any internal pressure (p = 0 kPa), the highest tensile contact stress is observed at the four corners, resembling square contact of solid pillars (Luo et al., 2020). However, when internal pressure is applied (p = 8 kPa), a ring-shape region with high tensile contact stress forms inside the contact area (Fig. 11(a)). This enclosed region increases the overall interfacial adhesive force when the contact stress at corners reaches the interfacial failure criterion, consistent with the adhesion enhancement observed in circular and elliptical contacts under positive pressure. As a result, the pull-off strength σ_p exhibits a monotonic increase from 4.53 kPa to 8.00 kPa measured in experiments within this pressure range.

Internal Crack

As the internal positive pressure is further increased beyond 16 kPa, the ring-like inner region with high tensile contact stress expands towards the center of the contact area, and the contact stress along the contact outline becomes compressive (p = 24 kPa, Fig. 11(a)). In this pressure regime, the pull-off strength keeps decreasing until it falls below 0.045 kPa when p reaches 24 kPa in experiments. The switching ratio is thus calculated as 100 ×. Furthermore, the delamination initiation site shifts from the corners to locations inside the contact area. Specifically, the interfacial crack initiates in a region close to the corners and then propagates slowly through the inner ring-shape region with retraction, as observed in both experiment and simulations (p = 24 kPa, Fig. 10(b)). After the ring-shape region is detached, the front of the interfacial crack steadily spreads towards the four edges and the center of the contact area with continuing retraction before the complete interfacial failure.

Crack at Midpoints of Edges

Under negative internal pressure, the four facets of the sidewall collectively bend inward, exerting a detaching moment on the contact membrane at the contact edge. Since the facet deforms more around its center than its 90-degree sharp edge, it is expected that the delamination initiation site shifts from the corners to positions near the midpoints of the four straight contact edges. Indeed, the contact normal stress distribution along the edges when the interfacial delamination begins shows that the highest contact normal stress appears close to the midpoints (p = -12 kPa, Fig. 11(b)-(c)). Consequently, the interfacial delamination initiates close to the midpoints of the four edges as observed by both experiments and simulations (p = -12 kPa, Fig. 10(c)). As the retraction process continues, the crack fronts spread along the contact outline and meet each other at the corners. This merging of cracks at the corners results in a sudden change in the interactive force F,

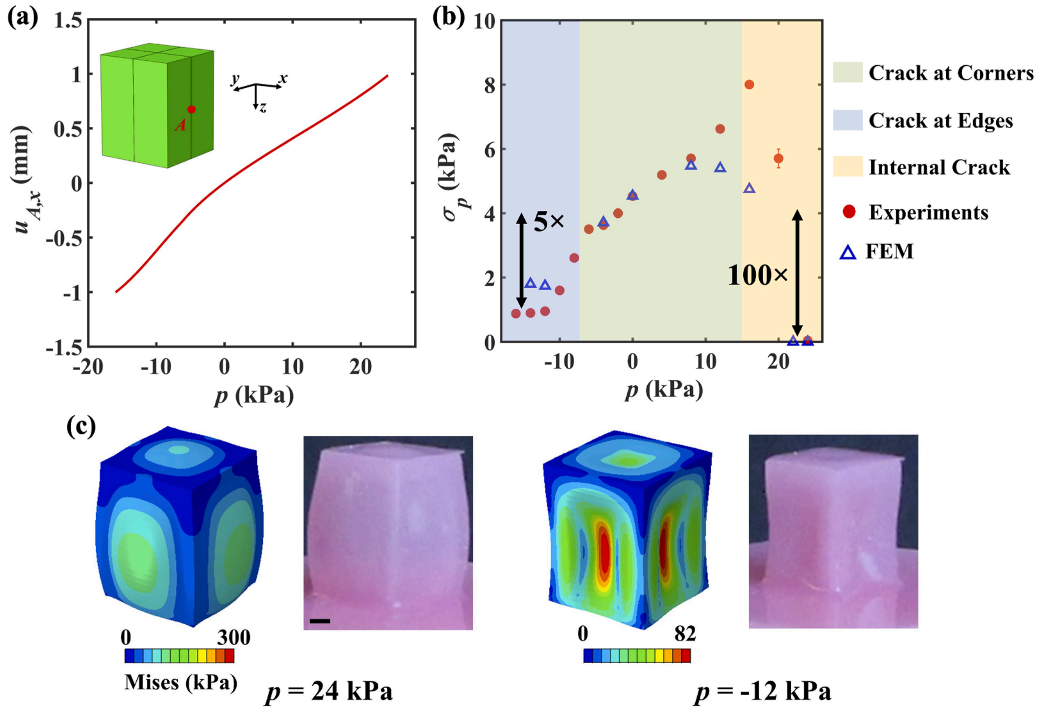

Fig. 9. (a) Displacement of center A of one facet along x axis $u_{A,x}$ with internal pressure p in FEM simulations. (b) Relationship between pull-off strength σ_p and internal pressure p of square contact in experiments (red circles) and simulations (blue triangles). The plot is divided into three regimes based on interfacial delamination behaviors. (c) Deformation of a square SHP with $l = w = 4.71$ mm under internal pressure $p = 24$ kPa and -12 kPa in simulations (left) and experiments (right). The scale bar is 1 mm.

observed in both experiment and simulations (Fig. 10(c), green box). After the interface fails along the square contact outline, the interfacial crack front continues to propagate towards the center until the interface experiences total failure.

Impacted by the sidewall bending, the pull-off strength experiences a consistent decline as the pressure magnitude increases. However, it is observed that σ_p levels off at around 0.88 kPa when the pressure magnitude surpasses 12 kPa (Fig. 9(b)) in experiments. Such a low switching ratio of 5 × is attributed to the absence of buckling instability caused by the 90-degree sharp edges. Consequently, the square SHP solely relies on the local deformation of its sidewall to assist in detachment of the contact membrane from the substrate, thus lacking the potential for significant reduction in adhesion strength.

4.2. Rectangular contact with $l/w = 1.3$

Square contact geometry introduces distinctive adhesive characteristics due to the presence of 90-degrees sharp corners and edges, setting it apart from circular or elliptical contacts. However, its deformation and contact delamination keep 90° rotational symmetry due to the equal length l and width w. To expand the design space and explore the influence of side length ratios l/w on adhesion, we extend our investigation to rectangular contact geometry with a specific ratio of $l/w = 1.3$. To maintain a consistent circumference c, we select length l and width w values as $l = 5.5$ mm and $w = 3.92$ mm, respectively.

The simulations show that the sidewall of a rectangular SHP bends outwards/inwards under internal positive/negative pressure, and the long facet experiences more deformation than short facet in the absence of 90° rotational symmetry (Fig. C3, Fig. C4(a)). Nevertheless, in the negative pressure regime, the rectangular SHP does not buckle globally, similar to the square SHP. When $p <$ -10 kPa, the sidewall deformation halts as the two long facets contact each other ($p =$ -12 kPa, Fig. C4(a), inset).

The same three interfacial delamination behaviors are also observed when the aspect ratio $l/w = 1.3$ (Fig. C4(b)). Within the pressure range 0 kPa $< p <$ 16 kPa, the initiation of delamination takes place at the corners of the contact outline, and the interfacial crack quickly propagates toward the central region of contact area ($p = 8$ kPa, Fig. C5(a)). Within this range of internal pressure, the pull-off strength σ_p initially increases with increasing pressure and then reaches a plateau around 8 kPa when the pressure p exceeds 4 kPa, in contrast with the monotonic trend in the square contact case. When the internal pressure is beyond 16 kPa, the delamination initiation site shifts to locations inside the contact area ($p = 20$ kPa, Fig. C5(b)). The interfacial cracks form at locations near the corners, followed by their propagation along the ring-shape region with high tensile contact stress. Then the crack front extends across the remaining contact area until the interface fails. In this regime, the pull-off strength σ_p begins to decrease with increasing pressure and drops below 0.0464 kPa when the pressure reaches 28 kPa in experiments. Consequently, the dry adhesion switching ratio is calculated to be 143 ×.

The third interfacial delamination behavior appears when the internal pressure is negative. In this case, delamination initiates around the midpoints of the two long edges since the long facets bend more significantly than the short facets (Fig. C5(c)). Due to the sidewall bending, σ_p exhibits a continuous decrease in magnitude as the negative pressure magnitude increases. Ultimately, σ_p reaches a plateau value of 1.02 kPa in experiments (Fig. C4(b)), resulting in a switching ratio of 7 ×. Similar to the square SHP, the rectangular SHP with $l/w = 1.3$ has a limited capacity in reducing adhesion strength through the application of internal negative pressure because of the absence of buckling instability.

5. Performance overview

In this section, we summarize and compare the tunable adhesion performance of SHPs with circular, elliptical, square, and rectangular contact geometries. The aim is to identify the best candidate that can effectively achieve reversible dry adhesion. Our analysis mainly focuses on key tunable adhesion performance metrics including adhesion

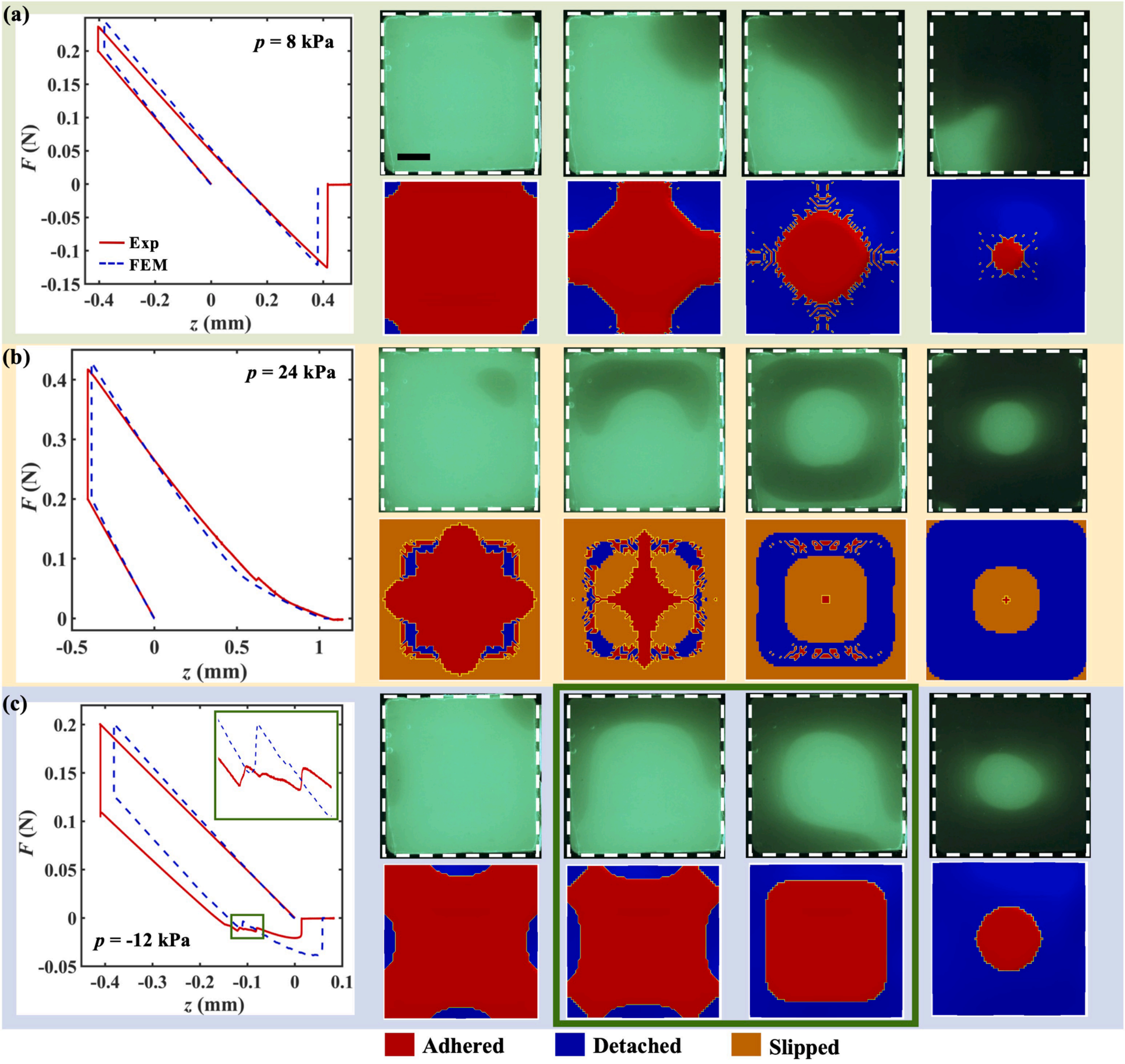

Fig. 10. Force F - displacement z curve and contact area evolution during adhesion test in both experiment (red solid curves) and simulation (blue dashed curves) for square contact geometry. Three interfacial delamination behaviors are (a) edge crack at corners (p = 8 kPa), (b) internal crack (p = 24 kPa), and (c) edge crack at midpoints of four edges (p = -12 kPa). The white dash line marks contact outline in experiment in the first row, and simulation is shown in the second row. The green box highlights the abrupt change of interactive force F. The scale bar is 1 mm.

strength, switching ratio, and activating pressure, as these metrics are essential for various applications, including tasks such as pick-and-place operations (Table 1). To ensure consistency, we have selected the adhesion strength value at zero internal pressure (p = 0 kPa) to evaluate the adhesion strengths of the SHPs with various contact geometries. All data is based on experimental measurement.

As summarized in Table 1, it becomes evident that the choice of contact geometry for the SHPs exerts minimal influence on the adhesion strength when the sidewall thickness t and contact circumference c are held constant. Across all considered contact geometries, SHPs exhibit a relatively uniform adhesion strength σ_p of approximately 5 kPa (4.66–6.63 kPa). Upon the application of positive pressure, SHPs of different contact geometries achieve adhesion switching ratios spanning two orders of magnitude. However, the required activating pressure magnitude is substantially higher compared to the negative pressure scenario (~10 kPa vs. ~ 20 kPa). In addition, under negative pressure only circular or elliptical contacts with low eccentricity (e.g., e = 0.64) can achieve switching ratios of two orders of magnitude owing to buckling instability. However, for SHPs with elliptical contacts with larger eccentricities (e.g., e = 0.87), the presence of self-contact in their sidewalls upon buckling hampers their efficacy in reducing adhesion strength, and thus leading to much lower adhesion switching ratios. For SHPs with square and rectangular contacts, the absence of sidewall buckling instability due to the 90-degree sharp edges contributes to their limited adhesion switching ratio under negative pressure.

The above analysis based on data summarized in Table 1 underscores the superiority of circular and elliptical (with small eccentricity) contact geometries for SHP design, given their impressive combination of a high adhesion switching ratio and a low activating pressure. However, it's worth emphasizing that the introduction of eccentricity to the contact geometry offers an additional advantage, namely, the ability to control sidewall buckling direction under negative pressure. For a SHP with elliptical contact, buckling dimples are always formed at its co-vertexes. In contrast, for a circular SHP, the formation of buckling dimples is sensitive to random defects introduced by the manufacturing process or misalignment during adhesion pull-off, and thereby is also random. This aspect gains particular significance when multiple SHPs are organized into patterns.

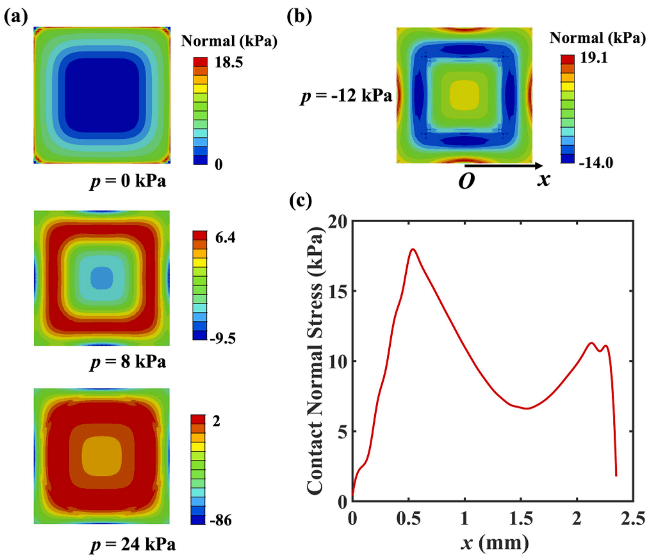

Fig. 11. (a) Contact normal stress distributions over square contact area when internal pressure p is 0 kPa, 8 kPa and 24 kPa in FEM simulations. (b) Contact normal stress distribution over square contact area under negative pressure $p =$ -12 kPa in simulations. (c) Contact normal stress distribution along one edge (x axis) when internal pressure $p =$ -12 kPa in simulations.

Table 1
Adhesion strength σ_p ($p = 0$ kPa), switching ratio and activating pressure of circular, elliptical, square, and rectangular contact geometry.

Contact Geometry	σ_p(kPa) ($p = 0$ kPa)	Switching Ratio ($p < 0$ kPa)	Activating Pressure (kPa) ($p < 0$ kPa)	Switching Ratio ($p > 0$ kPa)	Activating Pressure (kPa) ($p > 0$ kPa)
Circular	4.66	131×	-10	131×	20
Elliptical ($e = 0.64$)	6.55	182×	-8	182×	26
Elliptical ($e = 0.87$)	5.54	10×	-6	129×	24
Square ($l/w = 1$)	4.53	5×	-12	100×	24
Rectangular ($l/w = 1.3$)	6.63	6×	-10	143×	28

As evidence, we conduct FEM simulations to study the scenario of four circular SHPs arranged in a 2 × 2 pattern. Each SHP has dimensions of $d = 6$ mm, $h = 6$ mm, $t_s = t_b = 0.8$ mm, $t_p = 2$ mm. The distance between centers of adjacent SHPs is set to be 9 mm. Under negative pressure ($p =$ -10 kPa), these circular SHPs undergo sidewall buckling, and intriguingly, the buckling directions of adjacent SHPs are perpendicular to each other (Fig. 12(a)). The underlying reason is that the buckling dimple in a circular SHP generates a region with high stress magnitude in the top membrane. If two neighboring circular SHPs have identical buckling directions, these high-stress regions will intersect, leading to much increased elastic energy of the system. Consequently, a configuration where the adjacent dimples avert facing each other evolves as the preferred state, thereby resulting in non-uniform, unpredictable buckling directions for the assembled circular SHPs. However, for SHPs with elliptical contact geometries under the same negative pressure ($p =$ -10 kPa), their assembly exhibits a uniform buckling direction. This uniformity can be attributed to the predetermined locations of buckling dimples at the co-vertexes of the elliptical contacts (Fig. 12(b)). While it's true that two adjacent dimples face each other in this scenario, it is still energetically favorable for the assembled system of SHPs. This uniformity in buckling direction could offer distinct advantages in applications such as large-scale, parallel pick-and-place operations, as it ensures that the interfacial crack initiation site remains consistent for each object, potentially streamlining and optimizing the process, and increasing the spatial accuracy of object placement.

Another important observation to note is that an elliptical SHP needs roughly the same activating pressure as that of a circular SHP under internal negative pressure. This is in contrast with the fact that the buckling pressure p_{cr} of an elliptical SHP (~4 kPa) is much lower than that of a circular SHP (~10 kPa). Despite the lower pressure required for an elliptical SHP to initiate sidewall buckling, the resulting elastic force generated by the contact membrane at this initiating pressure is insufficient to detach it from the substrate. Therefore, the application of a much larger pressure magnitude than its initial buckling pressure becomes necessary to achieve a substantial reduction in adhesion strength.

6. Conclusion

In this work, through a combination of experiments and finite element modelling, we examine the adhesive behaviors of SHPs with various contact geometries including elliptical, square, and rectangular and compare them with circular SHPs. The findings reveal that, for SHPs with identical sidewall thickness and contact circumference, the adhesion strength remains relatively consistent across different contact geometries. Under positive pressure, SHPs with all contact geometries exhibit a switching ratio of two orders of magnitude, although the activating pressure required is higher than that under negative pressure. Under negative pressure, SHPs with circular and elliptical contact geometries demonstrate switching ratios of two orders of magnitude, owing to the sidewall buckling instability. However, as the eccentricity of the elliptical contact geometry increases, the switching ratio decreases significantly because of the contact of the buckling dimples. Conversely, SHPs with square or rectangular contact geometry exhibit

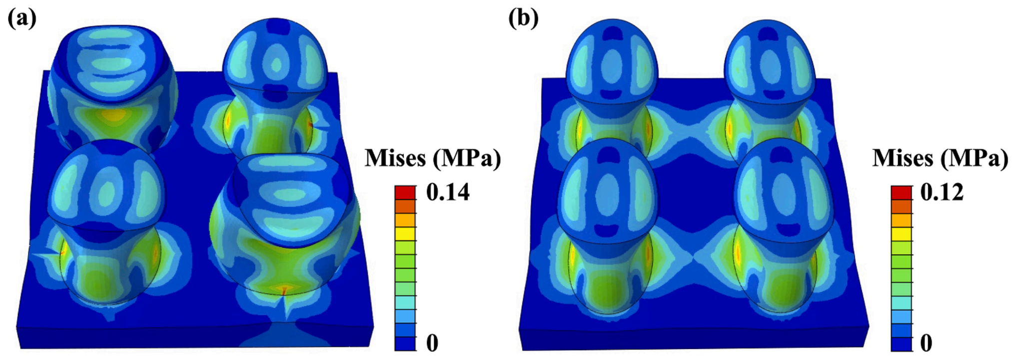

Fig. 12. FEM simulation results for buckled SHPs of a 2 × 2 pattern with (a) circular and (b) elliptical contact geometries.

limited adhesion switching ratio under negative pressure due to the absence of buckling instability. A comparative analysis between circular and elliptical (small eccentricity) contact geometries reveals similar adhesion strength, activating pressure, and switching ratio. However, a unique advantage becomes apparent when considering elliptical geometry for patterned assemblies of SHPs. Unlike circular SHPs, elliptical SHPs exhibit uniform buckling direction when arranged in patterns. This feature could prove advantageous for large-scale pick-and-place operations.

The significance of this work extends beyond its immediate scope. By unravelling the intricate nonlinear effects of sidewall and contact membrane deformations of SHPs with various contact geometries under internal pressure, this study enriches the design possibilities of SHPs. Furthermore, the insights gained herein could catalyze advancements in related domains such as transfer printing, robotic locomotion, and manipulation, where the choice of contact geometry can wield substantial influence. In sum, this investigation contributes profoundly to the evolving landscape of soft adhesive structures and their practical applications.

CRediT authorship contribution statement

Guangchao Wan: Writing – original draft, Validation, Investigation, Formal analysis. **Wanliang Shan:** Writing – review & editing, Supervision, Project administration, Investigation, Funding acquisition, Conceptualization.

Declaration of competing interest

The authors declare that they have no known competing financial interests or personal relationships that could have appeared to influence the work reported in this paper.

Data availability

Data will be made available on request.

Acknowledgement

This work was supported by National Science Foundation under awards CMMI #2006430 and #2239507 (G. W. and W. S.), as well as Syracuse University through startup funds (W. S.), The authors also thank Prof. Teng Zhang at Syracuse University, Prof. Kevin T. Turner at University of Pennsylvania and Prof. Rong Long at University of Colorado, Boulder for helpful discussions about the presentation of simulation results.

During the preparation of this paper, the authors used ChatGPT 3.5 to retouch the text. After using this tool/service, the authors reviewed and edited the content as needed and take full responsibility for the content of the publication.

Appendix A. Cohesive interaction setup in FEM

For a pair of nodes that become separated, the projection of their displacement along the normal and two tangential directions are denoted as δ_n, δ_s and δ_t, respectively (Fig. 2(d)). Here, the subscripts n, s and t correspond to the components in the normal and two tangential shear directions, respectively. Prior to the initiation of interfacial damage, the interfacial traction stress is linearly related to the separation in an uncoupled manner as:

$$\begin{aligned} \tau_n &= K_{nn}\delta_n \\ \tau_s &= K_{ss}\delta_s \\ \tau_t &= K_{tt}\delta_t \end{aligned} \tag{A.1}$$

where τ_n, τ_s and τ_t are the normal and shear components of the interfacial traction, and K_{nn}, K_{ss} and K_{tt} are the stiffness along the normal and two tangential directions. In our model, we choose $K_{nn} = 4$ MPa/mm, $K_{ss} = K_{tt} = 6$ MPa/mm. As the magnitude of the interfacial traction keeps increasing, it will meet the criterion of damage initiation, after which the cohesive response begins to degrade before the bonding totally fails. The quadratic traction criterion is chosen, which specifies that the damage is initiated when

$$\left(\frac{\tau_n}{\tau_n^0}\right)^2 + \left(\frac{\tau_s}{\tau_s^0}\right)^2 + \left(\frac{\tau_t}{\tau_t^0}\right)^2 = 1 \tag{A.2}$$

where the terms $\tau_n^0 = 0.02$ MPa, $\tau_s^0 = \tau_t^0 = 0.03$ MPa in the simulation. After the damage initiation criterion is reached, the cohesive interaction is degraded following the damage evolution law as

$$\begin{aligned} \tau_n &= (1-D)\overline{\tau_n} \\ \tau_s &= (1-D)\overline{\tau_s} \\ \tau_t &= (1-D)\overline{\tau_t} \end{aligned} \tag{A.3}$$

where D is the scalar damage variable that evolves from 0 to 1 as the degradation evolves from damage initiation to total failure. $\overline{\tau_n}$, $\overline{\tau_s}$ and $\overline{\tau_t}$ are the contact normal and shear stresses predicted by the linear elastic traction-separation law based on the current separation without damage. By defining the effective separation δ_m as $\delta_m = \sqrt{(\delta_n)^2 + (\delta_t)^2 + (\delta_s)^2}$, the scalar damage variable is defined as

$$D = \frac{\delta_m^f\left(\delta_m^{max} - \delta_m^0\right)}{\delta_m^{max}\left(\delta_m^f - \delta_m^0\right)} \tag{A.4}$$

where $\delta_m^f = 0.01$ mm is the effective separation at complete interfacial failure, δ_m^0 is the effective separation at the damage initiation, and δ_m^{max} is the maximum value of the effective separation during the loading history. To help convergence during the interfacial delamination, we assign the viscosity coefficient as 0.01. For other contact properties, the normal contact is set as "hard" contact while the tangential behavior is frictionless. For the general contact kinematics, we set the sliding formulation as finite sliding while the discretization method is chosen as "node-to-surface". As will be shown later, in addition to the contact between the contact membrane and the substrate, the sidewall will have self-contact driven by internal pressure. In these situations, a general contact formulation is employed by predefining the surface pairs, and the contact properties are configured to be hard normal contact without friction. The cohesive interaction is not set up for these interactions to reduce computational cost.

Appendix B. Adhesion of circular SHPs

The adhesive behaviors of circular SHPs are introduced for convenience. We made another batch of samples so the experimental measurement is slightly different from our previous report (Wan et al., 2022). The relationship between σ_p and p is shown in Fig. B1(a), and three types of delamination behaviors are identified.

The first type is edge crack (- 10 kPa $< p <$ 16 kPa, Fig. B1(c), middle). In this regime, σ_p increases from 3.63 kPa to 5.4 kPa when p increases from -8 kPa to 14 kPa in experiment. This pull-off strength enhancement results from the sidewall bending that effectively changes the distribution of contact stress. When negative internal pressure is applied, the sidewall bends inwards, which facilitates the opening of interfacial cracks at the edge of the contact area (Fig. B1(b)). However, when internal pressure p is positive ($p = 12$ kPa), the sidewall is inflated outward, exerting a bending moment on the bottom membrane at the edge. This bending moment suppresses the tensile contact normal stress at the edge while generating a new peak of tensile normal stress near the edge (Fig. B1(b)). Evidence can be found in contact normal stress distribution along the radial coordinate r in simulations (Fig. B1(c), middle).

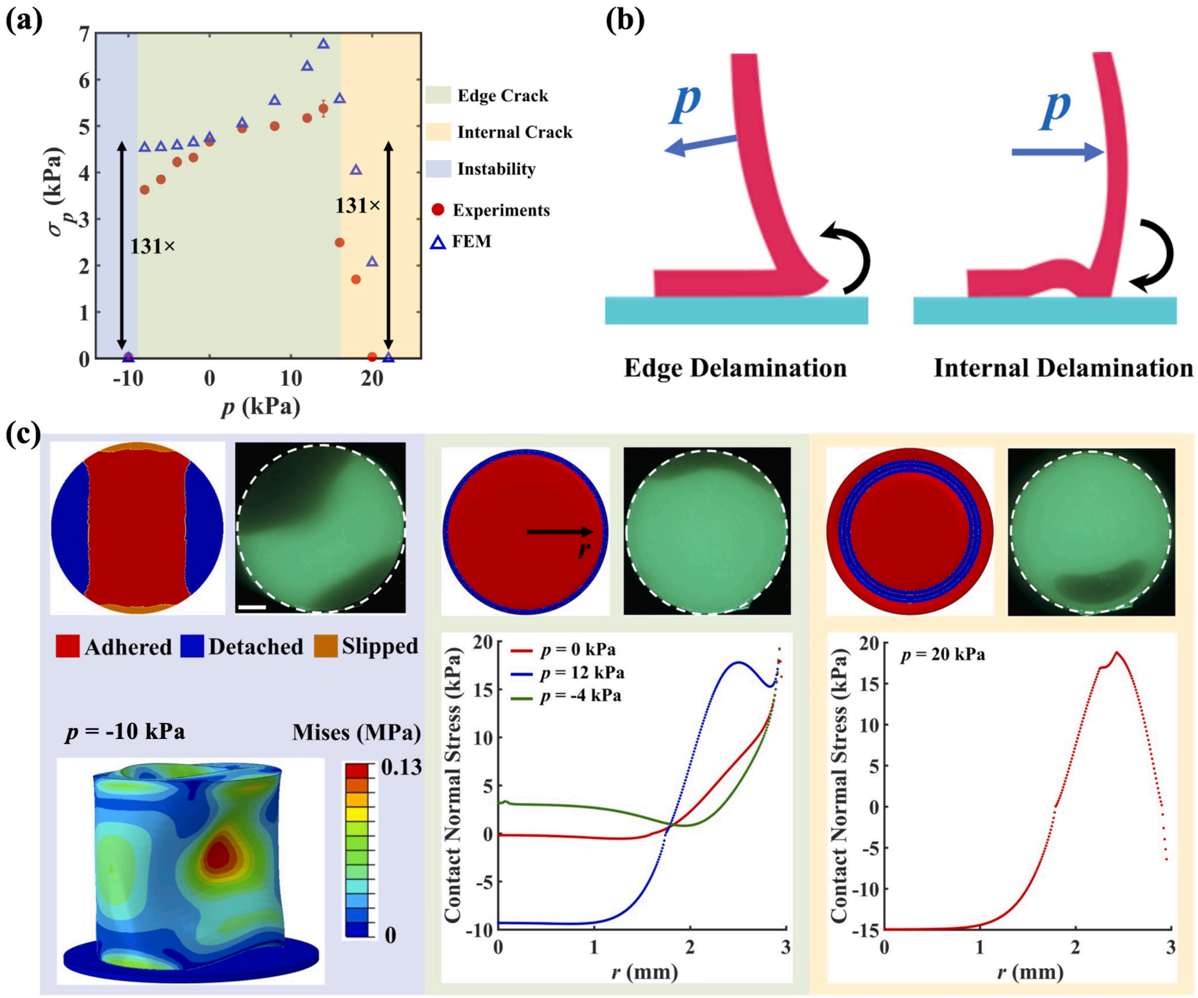

Fig. B1. (a) Relationship between pull-off strength σ_p and internal pressure p of a circular SHP from experiments (red circles) and simulations (blue triangles). (b) Schematic illustration of the effects of sidewall bending on interfacial delamination. (c) Buckling-induced interfacial crack (p = -10 kPa, left), interfacial edge crack with no-buckling (p = -4, 0, 12 kPa, middle) and interfacial internal crack (p = 20 kPa, right) from both experiments and simulations. The buckled shape of a SHP (p = -10 kPa) and the contact normal stress distributions along the radial direction in simulations are also shown. The scale bar is 1 mm.

When $p >$ 16 kPa, interfacial delamination occurs within the contact area (Fig. B1(c), right). In experiments, the crack first slowly propagates along the circumferential direction inside the contact outline, then spreads to the edge and finally moves towards the center (Fig. B2). In this situation, the pull-off force mainly comes from the adhesion of an inflated bottom membrane and the flat substrate, and thus becomes insignificant. Therefore, σ_p rapidly declines to a negligible value (0.035 kPa) when p reaches 20 kPa. Accordingly, the circular contact exhibits a switching ratio of 131 × when positive pressure is applied, and the activating pressure is 20 kPa. The shift of delamination site is attributed to changes in the distribution of contact stress (Fig. B1(c), right).

The circular SHP buckles when $p < p_c =$ -10 kPa. Two dimples form along the sidewall (Fig. B1(c), left), and the bottom membrane detaches from the substrate and deforms into a saddle shape. Immediately, the interface fails at two opposite sites at the edge, and these two edge cracks rapidly propagate toward each other until they merge, leaving only two disconnected, small interfacial regions that remain adhered (Fig. B1(c), left, Fig. B2). The significant reduction in contact area leads to negligible σ_p (0.035 kPa). Therefore, if negative pressure is applied, the circular contact has a switching ratio of 131×, and the magnitude of the activating pressure is 10 kPa.

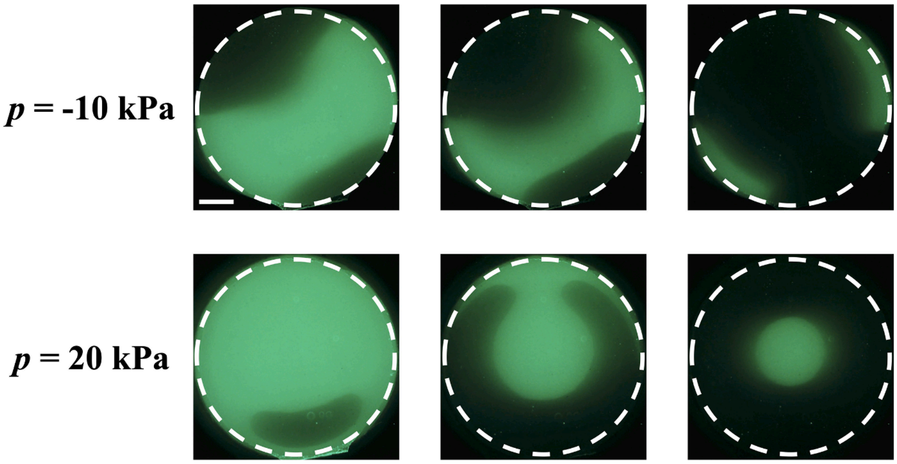

Fig. B2. Contact area evolution of an SHP with circular contact when internal pressure p = -10 kPa and 20 kPa in experiment. The white dash line denotes the contact outline. The scale bar is 1 mm.

Appendix C. Additional Figures for Elliptical, square and rectangular contact

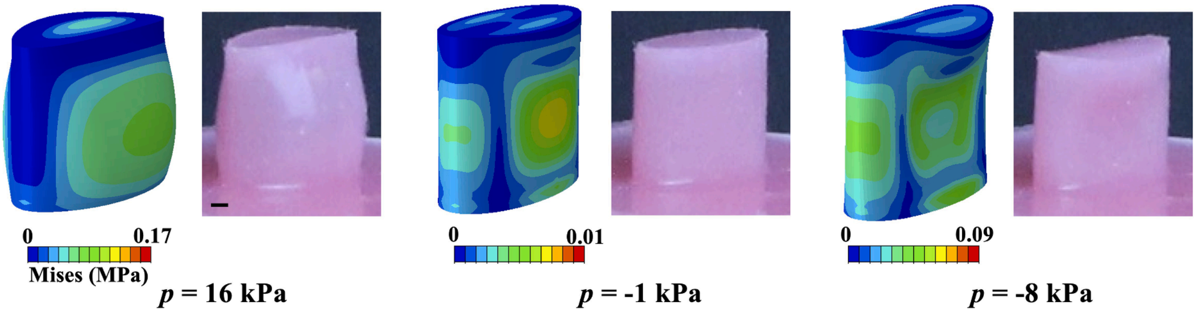

Fig. C1. Deformation of an elliptical SHP with $e = 0.87$ under internal pressure $p = 16$ kPa, -1 kPa and -8 kPa in simulations (left) and experiments (right). The scale bar is 1 mm.

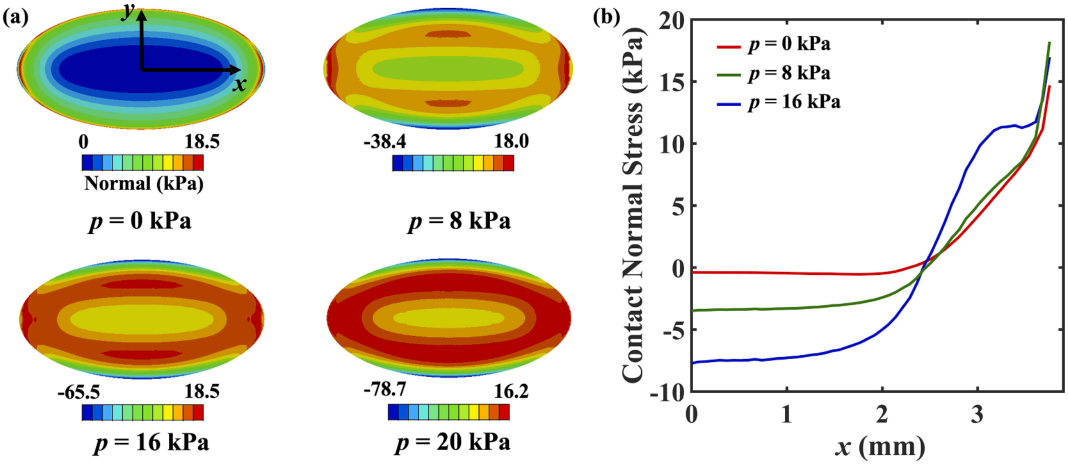

Fig. C2. (a) Contact normal stress distribution over contact area of an elliptical SHP in simulations ($e = 0.87$) when internal pressure p is 0 kPa, 8 kPa, 16 kPa and 20 kPa. (b) Contact normal stress distribution along the semi-major axis of elliptical contact area in simulations ($e = 0.87$) when internal pressure p is 0 kPa, 8 kPa and 16 kPa.

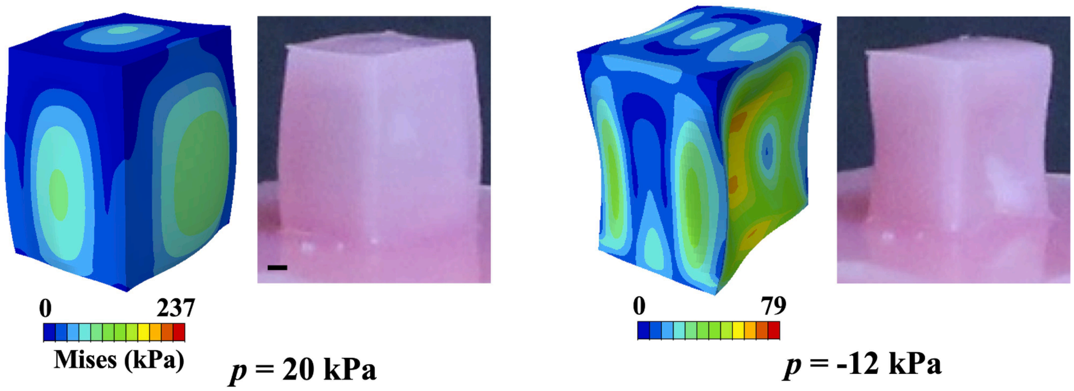

Fig. C3. Deformation of a rectangular SHP under internal pressure $p = 20$ kPa and -12 kPa in simulations (left) and experiments (right). The scale bar is 1 mm.

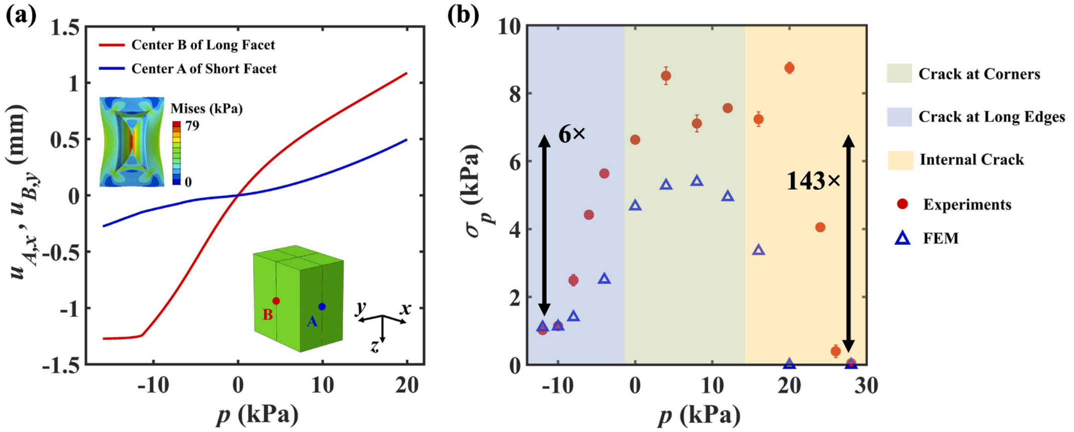

Fig. C4. (a) Displacement of center A of one short facet along x direction $u_{A,x}$ and displacement of center B of one long facet along y direction $u_{B,y}$ with internal pressure p in FEM simulations. The inset shows the contact of two long facets when p = -12 kPa in FEM simulations. (b) Relationship between pull-off strength σ_p and internal pressure p of rectangular contact ($l/w = 1.3$) in experiments (red circles) and simulations (blue triangles). The plot is divided into three regimes based on interfacial delamination behaviors.

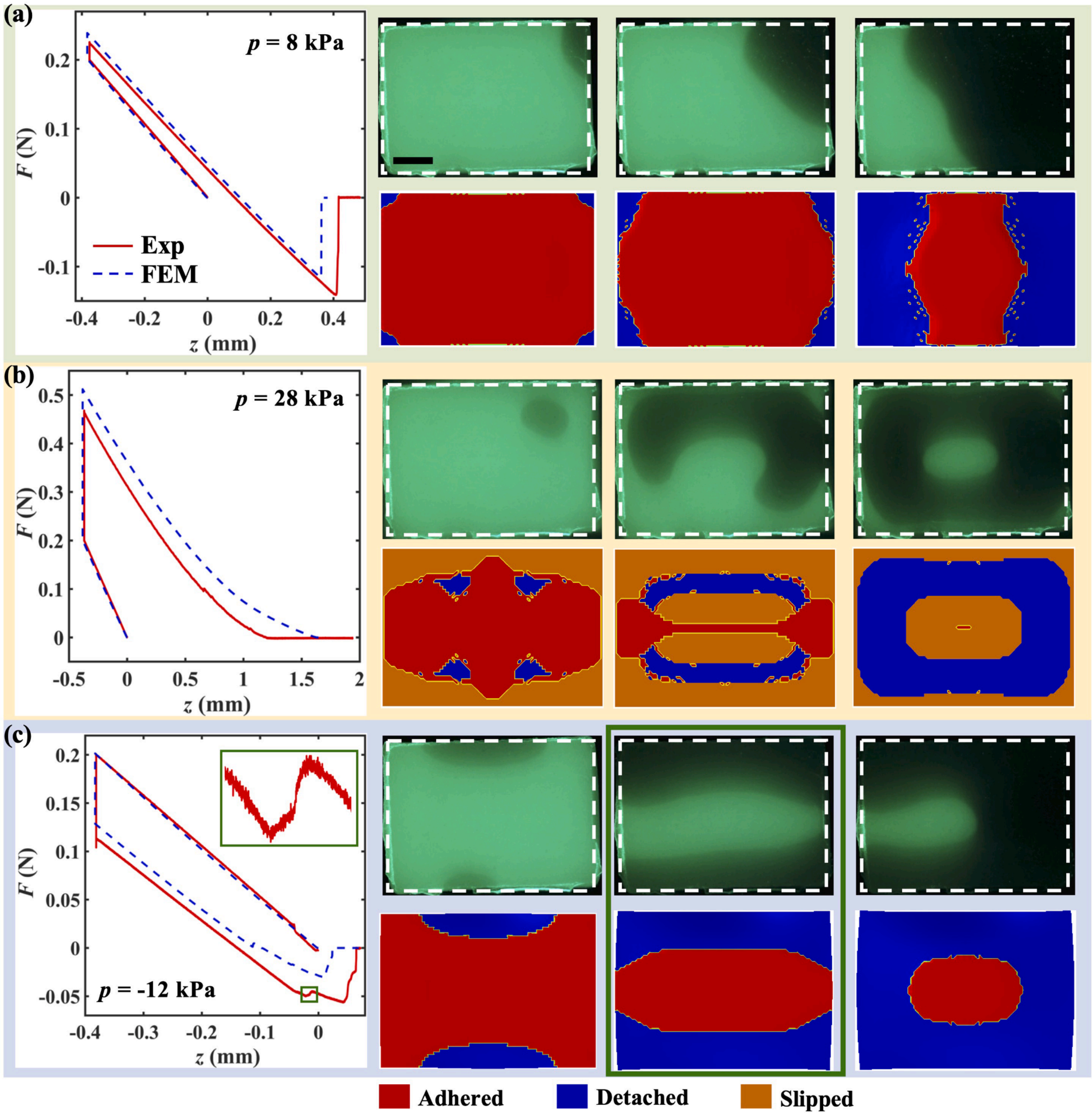

Fig. C5. Force *F* - displacement *z* curve and contact area evolution during adhesion test in both experiment (red solid curves) and simulation (blue dashed curves) for rectangular contact geometry ($l/w = 1.3$). Three interfacial delamination behaviors are (a) edge crack at corners ($p = 8$ kPa), (b) internal crack ($p = 24$ kPa), and (c) edge crack at midpoints of long edges ($p =$ -12 kPa). The white dash line marks contact outline in experiment in the first row, and simulation is shown in the second row. The green box indicates an abrupt change of interactive force *F*. The scale bar is 1 mm.

References

Areyano, M., Booth, J.A., Brouwer, D., Gockowski, L.F., Valentine, M.T., McMeeking, R. M., 2021. Suction-controlled detachment of mushroom-shaped adhesive structures. J. Appl. Mech. 88 https://doi.org/10.1115/1.4049392.

Autumn, K., Liang, Y.A., Hsieh, S.T., Zesch, W., Chan, W.P., Kenny, T.W., Fearing, R., Full, R.J., 2000. Adhesive force of a single gecko foot-hair. Nature 405, 681–685. https://doi.org/10.1038/35015073.

Balijepalli, R.G., Begley, M.R., Fleck, N.A., McMeeking, R.M., Arzt, E., 2016. Numerical simulation of the edge stress singularity and the adhesion strength for compliant mushroom fibrils adhered to rigid substrates. Int. J. Solids Struct. 85–86, 160–171. https://doi.org/10.1016/j.ijsolstr.2016.02.018.

Bartlett, M.D., Crosby, A.J., 2014. Material transfer controlled by elastomeric layer thickness. Mater. Horiz. 1, 507–512. https://doi.org/10.1039/C4MH00106K.

Carlson, A., Kim-Lee, H.-J., Wu, J., Elvikis, P., Cheng, H., Kovalsky, A., Elgan, S., Yu, Q., Ferreira, P.M., Huang, Y., Turner, K.T., Rogers, J.A., 2011. Shear-enhanced adhesiveless transfer printing for use in deterministic materials assembly. Appl. Phys. Lett. 98, 264104 https://doi.org/10.1063/1.3605558.

Carlson, A., Wang, S., Elvikis, P., Ferreira, P.M., Huang, Y., Rogers, J.A., 2012. Active, programmable elastomeric surfaces with tunable adhesion for deterministic assembly by transfer printing. Adv. Funct. Mater. 22, 4476–4484. https://doi.org/10.1002/adfm.201201023.

Cen, J., Komvopoulos, K., 2023. A cohesive-zone-based contact mechanics analysis of delamination in homogeneous and layered half-spaces subjected to Normal and shear surface tractions. J. Appl. Mech. 90 https://doi.org/10.1115/1.4062141.

Chen, M., Wu, Y., Chen, B., Tucker, A.M., Jagota, A., Yang, S., 2022. Fast, strong, and reversible adhesives with dynamic covalent bonds for potential use in wound dressing. Proceedings of the National Academy of Sciences 119, e2203074119. https://doi.org/10.1073/pnas.2203074119.

Cho, Y., Minsky, H.K., Jiang, Y., Yin, K., Turner, K.T., Yang, S., 2018. Shear adhesion of tapered nanopillar arrays. ACS Appl. Mater. Interfaces 10, 11391–11397. https://doi.org/10.1021/acsami.8b02303.

Coulson, R., Stabile, C.J., Turner, K.T., Majidi, C., 2021. Versatile Soft Robot Gripper Enabled by Stiffness and Adhesion Tuning via Thermoplastic Composite. Soft Robotics soro.2020.0088. https://doi.org/10.1089/soro.2020.0088.

Deneke, N., Booth, J.A., Chan, E.P., Davis, C.S., 2023. Self-assembled asperities for pressure-tunable adhesion. Adv. Mater. 35, 2207337. https://doi.org/10.1002/adma.202207337.

Drotlef, D.-M., Blümler, P., del Campo, A., 2014. Magnetically actuated patterns for bioinspired reversible adhesion (dry and wet). Adv. Mater. 26, 775–779. https://doi.org/10.1002/adma.201303087.

Frey, S.T., Haque, A.B.M.T., Tutika, R., Krotz, E.V., Lee, C., Haverkamp, C.B., Markvicka, E.J., Bartlett, M.D., 2022. Octopus-inspired adhesive skins for intelligent and rapidly switchable underwater adhesion. Sci. Adv. 8, eabq1905. https://doi.org/10.1126/sciadv.abq1905.

Glover, J.D., Yang, X., Long, R., Pham, J.T., 2023. Creasing in microscale, soft static friction. Nat Commun 14, 2362. https://doi.org/10.1038/s41467-023-38091-7.

B. Haverkamp, C., Hwang, D., Lee, C., D. Bartlett, M., 2021. Deterministic control of adhesive crack propagation through jamming based switchable adhesives. Soft Matter 17, 1731–1737. https://doi.org/10.1039/D0SM02129F.

Hensel, R., Moh, K., Arzt, E., 2018. Engineering micropatterned dry adhesives: from contact theory to handling applications. Adv. Funct. Mater. 28, 1800865. https://doi.org/10.1002/adfm.201800865.

Hwang, D., Lee, C., Yang, X., Pérez-González, J.M., Finnegan, J., Lee, B., Markvicka, E.J., Long, R., Bartlett, M.D., 2023. Metamaterial adhesives for programmable adhesion through reverse crack propagation. Nat. Mater. 1–9 https://doi.org/10.1038/s41563-023-01577-2.

Jagota, A., Hui, C.-Y., 2011. Adhesion, friction, and compliance of bio-mimetic and bio-inspired structured interfaces. Mater. Sci. Eng. R. Rep. 72, 253–292. https://doi.org/10.1016/j.mser.2011.08.001.

Johannes, K., Calahan, K., Bowen, L., Zuetell, E., Long, R., Rentschler, M., 2022. Mechanically switchable micro-patterned adhesive for soft material applications. Extreme Mech. Lett. 52, 101622 https://doi.org/10.1016/j.eml.2022.101622.

Kim, S., Wu, J., Carlson, A., Jin, S.H., Kovalsky, A., Glass, P., Liu, Z., Ahmed, N., Elgan, S. L., Chen, W., Ferreira, P.M., Sitti, M., Huang, Y., Rogers, J.A., 2010. Microstructured elastomeric surfaces with reversible adhesion and examples of their use in deterministic assembly by transfer printing. Proc. Natl. Acad. Sci. U.s.a. 107, 17095–17100. https://doi.org/10.1073/pnas.1005828107.

Koivikko, A., Drotlef, D.-M., Dayan, C.B., Sariola, V., Sitti, M., 2021. 3D-printed pneumatically controlled soft suction cups for gripping fragile, small, and rough objects. Advanced Intelligent Systems 3, 2100034. https://doi.org/10.1002/aisy.202100034.

Kwak, M.K., Jeong, H.E., Bae, W.G., Jung, H.-S., Suh, K.Y., 2011. Anisotropic adhesion properties of triangular-tip-shaped micropillars. Small 7, 2296–2300. https://doi.org/10.1002/smll.201100455.

Li, Q., Liu, W., Yang, C., Rao, P., Lv, P., Duan, H., Hong, W., 2022. Kirigami-inspired adhesion with high directional asymmetry. J. Mech. Phys. Solids 169, 105053. https://doi.org/10.1016/j.jmps.2022.105053.

Linghu, C., Liu, Y., Tan, Y.Y., Sing, J.H.M., Tang, Y., Zhou, A., Wang, X., Li, D., Gao, H., Hsia, K.J., 2023. Overcoming the adhesion paradox and switchability conflict on rough surfaces with shape-memory polymers. Proceedings of the National Academy of Sciences 120, e2221049120. https://doi.org/10.1073/pnas.2221049120.

Linghu, C., Zhang, S., Wang, C., Yu, K., Li, C., Zeng, Y., Zhu, H., Jin, X., You, Z., Song, J., 2020. Universal SMP gripper with massive and selective capabilities for multiscaled, arbitrarily shaped objects. Sci. Adv. 6, eaay5120. https://doi.org/10.1126/sciadv.aay5120.

Long, R., Hui, C.-Y., 2012. Axisymmetric membrane in adhesive contact with rigid substrates: analytical solutions under large deformation. Int. J. Solids Struct. 49, 672–683. https://doi.org/10.1016/j.ijsolstr.2011.11.008.

Long, R., Shull, K.R., Hui, C.-Y., 2010. Large deformation adhesive contact mechanics of circular membranes with a flat rigid substrate. J. Mech. Phys. Solids 58, 1225–1242. https://doi.org/10.1016/j.jmps.2010.06.007.

Luo, A., Mohammadi Nasab, A., Tatari, M., Chen, S., Shan, W., Turner, K.T., 2020. Adhesion of flat-ended pillars with non-circular contacts. Soft Matter 16, 9534–9542. https://doi.org/10.1039/D0SM01105C.

Luo, A., Pande, S.S., Turner, K.T., 2022a. Versatile adhesion-based gripping via an unstructured variable stiffness membrane. Soft Rob. 9, 1177–1185. https://doi.org/10.1089/soro.2021.0065.

Luo, A., Zhang, H., Turner, K.T., 2022b. Machine learning-based optimization of the design of composite pillars for dry adhesives. Extreme Mech. Lett. 54, 101695 https://doi.org/10.1016/j.eml.2022.101695.

Ma, Y., Ma, S., Wu, Y., Pei, X., Gorb, S.N., Wang, Z., Liu, W., Zhou, F., 2018. Remote control over underwater dynamic attachment/detachment and locomotion. Adv. Mater. 30, 1801595. https://doi.org/10.1002/adma.201801595.

Meitl, M.A., Zhu, Z.-T., Kumar, V., Lee, K.J., Feng, X., Huang, Y.Y., Adesida, I., Nuzzo, R. G., Rogers, J.A., 2006. Transfer printing by kinetic control of adhesion to an elastomeric stamp. Nature Mater 5, 33–38. https://doi.org/10.1038/nmat1532.

Minsky, H.K., Turner, K.T., 2015. Achieving enhanced and tunable adhesion via composite posts. Appl. Phys. Lett. 106, 201604 https://doi.org/10.1063/1.4921423.

Minsky, H.K., Turner, K.T., 2017. Composite microposts with high dry adhesion strength. ACS Appl. Mater. Interfaces 9, 18322–18327. https://doi.org/10.1021/acsami.7b01491.

Mohammadi Nasab, A., Luo, A., Sharifi, S., Turner, K.T., Shan, W., 2020. Switchable adhesion via subsurface pressure modulation. ACS Appl. Mater. Interfaces 12, 27717–27725. https://doi.org/10.1021/acsami.0c05367.

Mohammadi Nasab, A., Stampfli, P., Sharifi, S., Luo, A., Turner, K.T., Shan, W., 2022. Dynamically tunable dry adhesion through a subsurface thin layer with tunable stiffness. Adv Materials Inter 9, 2102080. https://doi.org/10.1002/admi.202102080.

Murphy, M.P., Aksak, B., Sitti, M., 2009. Gecko-inspired directional and controllable adhesion. Small 5, 170–175. https://doi.org/10.1002/smll.200801161.

Plaut, R.H., White, S.A., Dillard, D.A., 2003. Effect of work of adhesion on contact of a pressurized blister with a flat surface. Int. J. Adhes. Adhes. 23, 207–214. https://doi.org/10.1016/S0143-7496(03)00013-7.

Shi, J., Müftü, S., Wan, K.-T., 2011. Adhesion of an elastic convex Shell onto a rigid plate. J. Adhes. 87, 579–594. https://doi.org/10.1080/00218464.2011.583587.

Song, S., Sitti, M., 2014. Soft grippers using micro-fibrillar adhesives for transfer printing. Adv. Mater. 26, 4901–4906. https://doi.org/10.1002/adma.201400630.

Swift, M.D., Haverkamp, C.B., Stabile, C.J., Hwang, D., Plaut, R.H., Turner, K.T., Dillard, D.A., Bartlett, M.D., 2020. Active membranes on rigidity tunable foundations for programmable. Rapidly Switchable Adhesion. Adv. Mater. Technol. 5, 2000676. https://doi.org/10.1002/admt.202000676.

Tatari, M., Mohammadi Nasab, A., Turner, K.T., Shan, W., 2018. Dynamically tunable dry adhesion via subsurface stiffness modulation. Adv. Mater. Interfaces 5, 1800321. https://doi.org/10.1002/admi.201800321.

Testa, P., Chappuis, B., Kistler, S., W. Style, R., J. Heyderman, L., R. Dufresne, E., 2020. Switchable adhesion of soft composites induced by a magnetic field. Soft Matter 16, 5806–5811. https://doi.org/10.1039/D0SM00626B.

Tian, H., Li, X., Shao, J., Wang, C., Wang, Y., Tian, Y., Liu, H., 2019. Gecko-effect inspired soft gripper with high and switchable adhesion for rough surfaces. Adv. Mater. Interfaces 6, 1900875. https://doi.org/10.1002/admi.201900875.

Tian, H., Wang, D., Zhang, Y., Jiang, Y., Liu, T., Li, X., Wang, C., Chen, X., Shao, J., 2022. Core–shell dry adhesives for rough surfaces via electrically responsive self-growing strategy. Nat Commun 13, 7659. https://doi.org/10.1038/s41467-022-35436-6.

Tinnemann, V., Hernández, L., Fischer, S.C.L., Arzt, E., Bennewitz, R., Hensel, R., 2019. In situ observation reveals local detachment mechanisms and suction effects in micropatterned adhesives. Adv. Funct. Mater. 29, 1807713. https://doi.org/10.1002/adfm.201807713.

Wahdat, H., Elzière, P., Chan, N., Crosby, A.J., 2021. Mechanics of adhesives under annular confinement: internal pressure, force, and interfacial area. Soft Matter 17, 5540–5547. https://doi.org/10.1039/D1SM00089F.

Wan, K.-T., 2001. Adherence of an axisymmetric flat punch on a thin flexible membrane. J. Adhes. 75, 369–380. https://doi.org/10.1080/00218460108029611.

Wan, K.-T., Duan, J., 2002. Adherence of a rectangular flat punch onto a clamped plate: transition from a rigid plate to a flexible membrane. J. Appl. Mech. 69, 104–109. https://doi.org/10.1115/1.1432989.

Wan, G., Tang, Y., Turner, K.T., Zhang, T., Shan, W., 2022. Tunable dry adhesion of soft hollow pillars through sidewall buckling under low pressure. Adv Funct Materials 2209905. https://doi.org/10.1002/adfm.202209905.

Wang, D., Hu, H., Li, S., Tian, H., Fan, W., Li, X., Chen, X., Taylor, A.C., Shao, J., 2023. Sensing-triggered stiffness-tunable smart adhesives. science. Advances 9, eadf4051. https://doi.org/10.1126/sciadv.adf4051.

Wang, Y., Li, X., Tian, H., Hu, H., Tian, Y., Shao, J., Ding, Y., 2015. Rectangle-capped and tilted micropillar array for enhanced anisotropic anti-shearing in biomimetic adhesion. J. R. Soc. Interface. 12, 20150090. https://doi.org/10.1098/rsif.2015.0090.

Wang, C., Linghu, C., Nie, S., Li, C., Lei, Q., Tao, X., Zeng, Y., Du, Y., Zhang, S., Yu, K., Jin, H., Chen, W., Song, J., 2020. Programmable and scalable transfer printing with high reliability and efficiency for flexible inorganic electronics. Sci. Adv. 6, eabb2393. https://doi.org/10.1126/sciadv.abb2393.

Wu, Y., Dong, X., Kim, J., Wang, C., Sitti, M., 2022. Wireless soft millirobots for climbing three-dimensional surfaces in confined spaces. science. Advances 8, eabn3431. https://doi.org/10.1126/sciadv.abn3431.

Xue, L., Sanz, B., Luo, A., Turner, K.T., Wang, X., Tan, D., Zhang, R., Du, H., Steinhart, M., Mijangos, C., Guttmann, M., Kappl, M., del Campo, A., 2017. Hybrid surface patterns mimicking the Design of the Adhesive toe pad of tree frog. ACS Nano 11, 9711–9719. https://doi.org/10.1021/acsnano.7b04994.

Yang, X., Srivastava, A., Long, R., 2023. Adhesive contact of an inflated circular membrane with curved surfaces. Int. J. Solids Struct. 279, 112371 https://doi.org/10.1016/j.ijsolstr.2023.112371.

Yao, H., Gao, H., 2006. Mechanics of robust and releasable adhesion in biology: bottom–up designed hierarchical structures of gecko. J. Mech. Phys. Solids 54, 1120–1146. https://doi.org/10.1016/j.jmps.2006.01.002.

Zhang, X., Wang, Y., Tian, Z., Samri, M., Moh, K., McMeeking, R.M., Hensel, R., Arzt, E., 2022. A bioinspired snap-through metastructure for manipulating micro-objects. Sci. Adv. 8, eadd4768. https://doi.org/10.1126/sciadv.add4768.

Zhao, C., Chen, X., Shan, W., Wan, K., 2022a. Adherence of a hyperelastic shell on a rigid planar substrate. Int. J. Solids Struct. 236–237, 111351 https://doi.org/10.1016/j.ijsolstr.2021.111351.

Zhao, J., Li, X., Tan, Y., Liu, X., Lu, T., Shi, M., 2022b. Smart adhesives via magnetic actuation. Adv. Mater. 34, 2107748. https://doi.org/10.1002/adma.202107748.